We are IntechOpen,
the world's leading publisher of
Open Access books
Built by scientists, for scientists

4,800
Open access books available

122,000
International authors and editors

135M
Downloads

Our authors are among the

154
Countries delivered to

TOP 1%
most cited scientists

12.2%
Contributors from top 500 universities

WEB OF SCIENCE™

Selection of our books indexed in the Book Citation Index
in Web of Science™ Core Collection (BKCI)

Interested in publishing with us?
Contact book.department@intechopen.com

Numbers displayed above are based on latest data collected.
For more information visit www.intechopen.com

Segmentation Methods for Biomedical Images

Roberto Rodríguez Morales
Institute of Cybernetics, Mathematics & Physics (ICIMAF),
Digital Signal Processing Group
Cuba

1. Introduction

Nowadays biomedical imaging provides major aid in many branches of medicine; it enables and facilitates the capture, transmission and analysis of biomedical images as well as providing assistance towards medical diagnoses. Medical imaging is still on the rise with new imaging modalities being added and continuous improvements of devices' capabilities. Segmentation and contour extraction are important steps towards image analysis. Segmented images are now used routinely in a multitude of different applications, such as, diagnosis, treatment planning, localization of pathology, study of anatomical structure, computer-integrated surgery, among others. However, image segmentation remains a difficult task due to both the variability of object shapes and the variation in image quality. Particularly, biomedical images are often corrupted by noise and sampling artifacts, which can cause considerable difficulties when applying rigid methods.

In many occasions, segmentation is considered as a process of classification of objects in a scene, and also in certain measure, it is equivalent to its recognition (objects) since, as a consequence of segmentation the different objects (physical realizations of classes or abstract patterns), these stay perfectly located inside the digital image.

In a graphic way in Figure 1, it is represented the segmentation process of a simple image. It is appreciated in this Figure that as result of segmentation the image was transformed from a gross digital image with all their information in form of gray-levels to an image much more simplified, where the different objects are well distinguished.
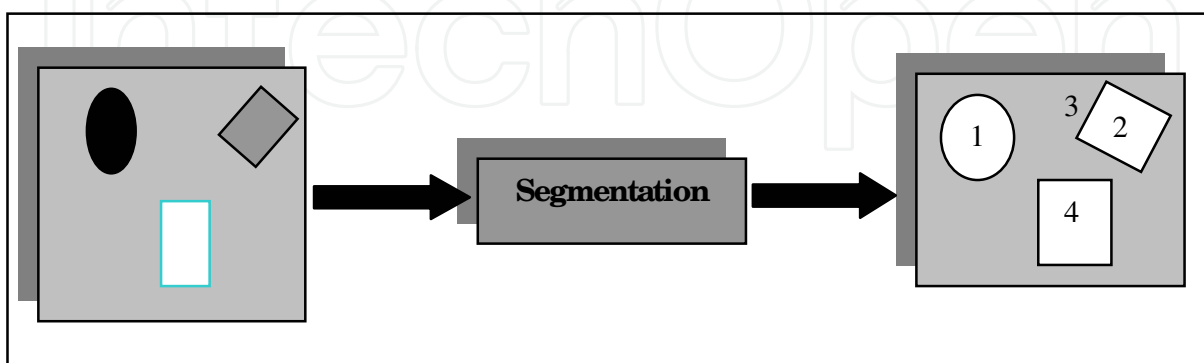

Fig. 1. Simple outline that represents the segmentation process

Many segmentation methods have been proposed for biomedical-image data [Chin-Hsing et al., 1998; Kenong & Levine, 1995; Koss et al., 1999; Rodríguez et al., 2002; Sijbers et al., 1997;

Schmid, 1999]. Unfortunately, segmentation using traditional low-level image processing techniques, such as thresholding, histogram and other classical operations, requires a considerable amount of interactive guidance in order to get satisfactory results. Automating these model-free approaches is difficult because of shape complexity, shadows, and variability within and across individual objects. Furthermore, noise and other image artifacts can cause incorrect regions or boundary discontinuities in objects recovered from these methods. However, it is accepted that despite the more complex algorithms developed so far, the segmentation of images remains highly dependent on the application and a single method has not yet been found that can solve all the problems in the universe.

In mathematical morphology (MM) important methods have been developed for image segmentation [Vicent & Soille, 1991; Vincent, 1993]. One of the most powerful tools developed in MM is the *Watersheds* transformation, which is classic in the field of topography and it has been used in many problems of image segmentation. However, the *Watersheds* transformation has the disadvantage of producing over-segmentation [Fuh et al., 1991; Najman & Schmitt, 1996]. For that reason, the correct way to use watersheds for grayscale image segmentation is to mark the regions we want to segment; that is, the objects, but also the background. One and only one marker must correspond to each region. The design of robust marker detection techniques involves the use of specific knowledge of the series of images under study.

Other technique very used in the last years for image segmentation is the mean shift, which is a non-parametric procedure for multimodal data analysis and has shown great superiority in many applications of high-level tasks [Comaniciu, 2000]. The mean shift was proposed in 1975 by Fukunaga et. al. [Fukunaga & Hostetler, 1975] and was largely forgotten until Cheng in 1995 rekindled interests in it [Cheng, 1995]. A computer model based on the mean shift procedure is an extremely versatile tool for feature analysis and can give a reliable solution for many tasks of computer vision [Comaniciu & Meer, 2002]. Segmentation by using the mean shift carries out a smoothing filter as a first step before segmentation is performed [Comaniciu, 2000].

The aim of this chapter is to present the advances that the author and their collaborators have obtained in the biomedical image segmentation. Also, some strategies that constitute appropriate tools are presented, which it can be used in many system of image analysis where methods of segmentation are required.

This chapter is structured as follows: In Section 2 the most significant theoretical aspects are detailed of each of the used methods in biomedical image segmentation. In Section 3 some of the characteristics of the studied images are described. In Section 4 the steps carried out in the experimentation are explained, and also an analysis and discussion of the proposed strategies is carried out. In this section two algorithms are presented to carry out the segmentation. Finally, in Section 5 the most important conclusions of this chapter are given.

2. Theoretical aspects

In mathematical morphology, it is usual to consider that grayscale images are often considered as topographic reliefs. In the topographic representation of a given image I, the numerical value (that is, the gray tone) of each pixel stands for the elevation at this point. Such a representation is extremely useful, since it allows one to better appreciate the effect of the different transformations on the image under study.

2.1 Morphological grayscale reconstruction

Now, it is given a group of definitions and concepts which are important for a better understanding of the proposed strategies.

Let us consider a two-dimensional grayscale picture **I** whose definition domain is denoted $D_I \subset Z^2$. **I** is supposed to take discrete (gray) values in a given range *[0, L-1]*, L being an arbitrary positive integer

$$I \begin{pmatrix} D_I \subset Z^2 & \to \{0, 1, 2, \ldots\ldots\ldots, L\text{-}1\} \\ p & \to I(p) \end{pmatrix} \tag{1}$$

Let **J** and **I** be two grayscale images defined on the same domain D_I, taking their values in the discrete set *{0, 1, ..., L-1}* and such that $J \leq I$ (i.e., for each pixel $p \in D_I$, $J(p) \leq I(p)$). In this way, it is useful to introduce the geodesic dilations according to the following definition [Vincent, 1993]:

Definition 2.1.1 (Geodesic dilation): The elementary geodesic dilation of $\delta_I^{(1)}(J)$ of grayscale image $J \leq I$, J "under" I (J is called the marker image and I is the mask) is defined as,

$$\delta_I^{(1)}(J) = (J \oplus B) \wedge I \tag{2}$$

where the symbol Λ stands for the pointwise minimum and $J \oplus B$ is the dilation of J by flat structuring element B. The grayscale geodesic dilation of size $n \geq 0$ is obtained by,

$$\delta_I^{(n)}(J) = \delta_I^{(1)} \circ \delta_I^{(1)} \circ \cdots \cdots \circ \delta_I^{(1)}(J), \; n \; times \tag{3}$$

Starting from the definition 2.1.1 and the expression (3) it can be derived an efficient definition for the morphological reconstruction of images in gray-levels.

Definition 2.1.2 (Grayscale reconstruction): The grayscale reconstruction $\rho_I^{(J)}$ of I from J is obtained by iterating grayscale dilations of J "under" I until stability is reached [Vincent, 1993], that is,

$$\rho_I(J) = \bigvee_{n \geq 1} \delta_I^{(n)}(J) \tag{4}$$

Definition 2.1.3 (Geodesic erosion): Similarly, the elementary geodesic erosion $\varepsilon_I^{(1)}(J)$ of grayscale image $J \geq I$, J "above" I is given by,

$$\varepsilon_I^{(1)}(J) = (J \, \theta \, B) \vee I \tag{5}$$

where $\vee$ stands for the pointwise maximum and $J \, \theta \, B$ is the erosion of J by flat structuring element B. The grayscale geodesic erosion of size n $\geq$ 0 is then given by,

$$\varepsilon_I^{(n)}(J) = \varepsilon_I^{(1)} \circ \varepsilon_I^{(1)} \circ \cdots \cdots \circ \varepsilon_I^{(1)}(J), n \; times \tag{6}$$

Definition 2.1.4 (Dual reconstruction): The dual grayscale reconstruction $\rho_f^*(J)$ of mask I from marker J is obtained by iterating grayscale geodesic erosions of J "above" I until stability is reached; that is,

$$\rho_I^*(J) = \bigwedge_{n \geq 1} \varepsilon_I^{(n)}(J) \tag{7}$$

Reconstruction turns out to provide a very efficient method to extract regional maxima and minima from grayscale images. Furthermore, the technique extends to the determination of maximal structures, which will be call *h-domes* and *h-basins*. The *h-domes* transformation extracts light structure without involving any size or shape criteria. The only parameter *(h)* is related to the height of these structures. The mathematical background and other definitions can be found in [Vincent, 1993].

2.1.1 Dome extraction and regional maxima

We consider the successive thresholds $T_h (I)$ of *I*, for *h = 0* to *L-1* [Vincent, 1993],

$$T_h(I) = \{ p \in D_I \, / \, I(p) \leq h \} \tag{8}$$

They are said to constitute the threshold decomposition of *I*, where these sets satisfy the following inclusion relationship:

$$T_h (I) \subseteq T_{h-1} (I) \qquad \forall \; h \in [0, L\text{-}1] \tag{9}$$

Definition 2.1.1.1 (Regional Minimum): A regional minimum *M* at altitude *h* of grayscale image *I* is a connected component *C* of $T_h (I)$ such that $C \cap T_{h-1} (I) = \varphi$, T_h (I) being a threshold of *I* at level *h* and the symbol φ stands for empty set.

Definition 2.1.1.2 (Regional maximum): A regional maximum at altitude h of grayscale image I is a connected component C de T_h (I) such that $C \cap T_{h+1}(f) = \varphi$.

In Figure 2 one can observe a representation of regional maxima in a grayscale image.
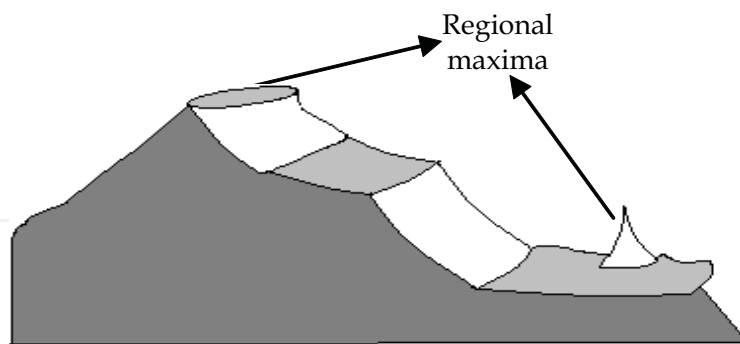

Fig. 2. Regional maxima in a grayscale image

Regional maxima should not be mistaken with local maxima. A pixel *p* of *I* is a local maximum for grid *H* if and only if its value *I (p)* is greater or equal to that of any of its neighbours. All the pixels belonging to a regional maximum are local maxima, but the converse is not true. For example, a pixel *p* belonging to the inside of a plateau is a local maximum, but the plateau may have neighbouring pixels of higher altitude and thus not be a regional maximum.

One of the most efficient methods makes use of grayscale reconstruction and is based on the following proposition.

Proposition 2.1.1.1: The (binary) image *M (I)* of the regional maxima of *I* is given by,

$$M(\,I\,) = f - \rho_I(\,I\,-\,1)$$

where $\rho_I(\,I\,-\,1)$, it is a morphological reconstruction (see definition 2.1.2, in this case $J = I\text{-}1)$. The proof of this proposition can be seen in [Vincent, 1993].
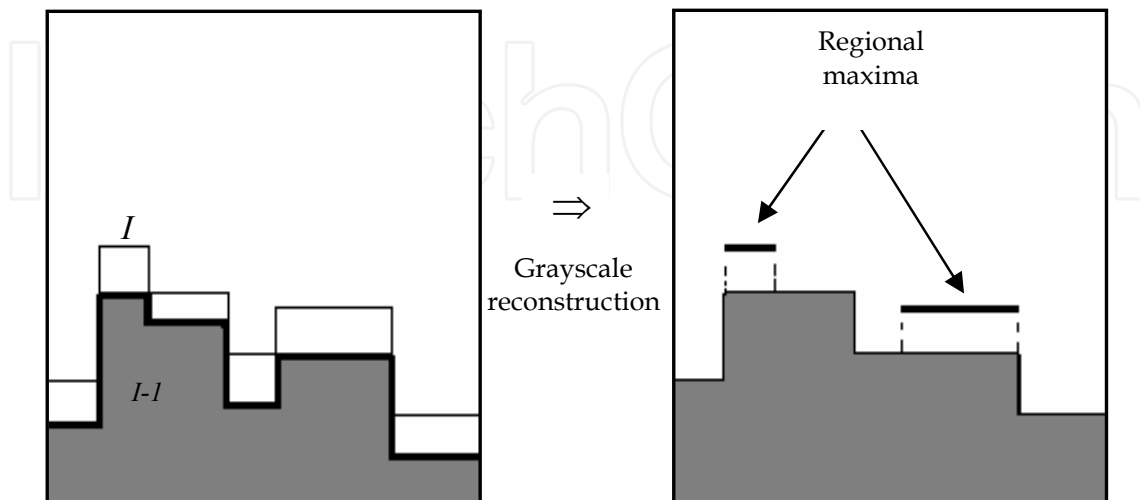For a better understanding of this proposition the same is illustrated in Figure 3.

Fig. 3. Extracting the regional maxima of I by reconstruction of I from *I-1*

The proposition 2.1.1.1 can be generalized and instead of subtracting value *1*, an arbitrary gray-level constant *h* can be subtracted from *I*. This provides a useful technique for extracting domes of a given height, which is called h-domes. Then, be the following definition:
Definition 2.1.1.3: The *h-dome* image $D_h\,(I)$ of the *h-domes* of a grayscale image *I* is given by

$$D_h\,(\,I\,) = I\text{-}\,\rho_I(\,I\,\,-h\,)$$

The *h-dome* transformation is illustrated on Figure 4. Unlike the classical transformation *Top-Hat*, the *h-dome* transformation extracts light structures without involving any size or shape criterion. The only parameter *(h)* is related to the height of these structures [Vincent, 1993].
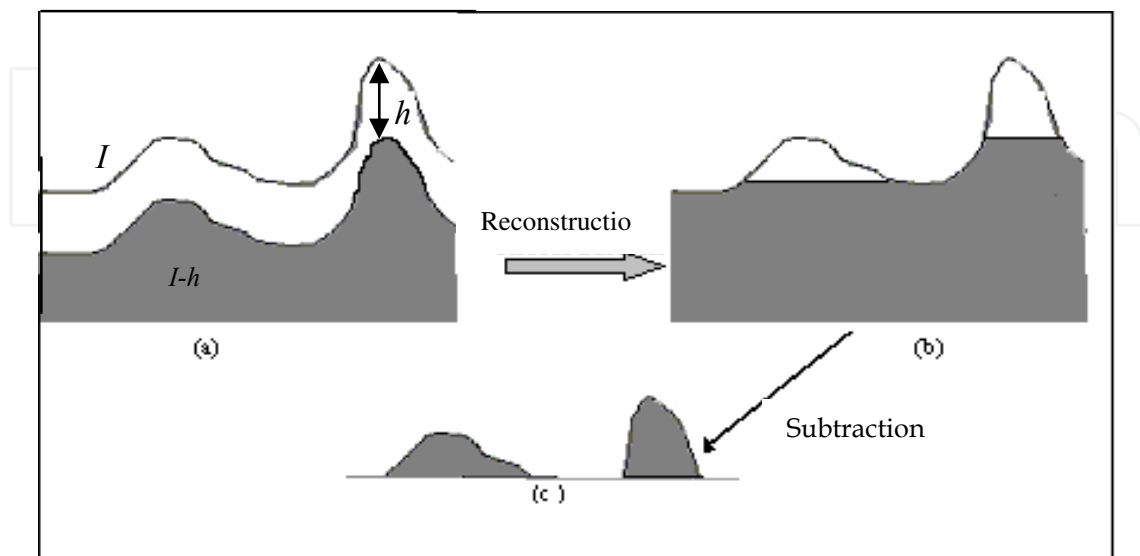

Fig. 4. Determination of the *h-domes* of grayscale image *I*

2.1.2 *Watershed* segmentation method

The *Watershed* segmentation consists in extracting objects from a gray-level image as precisely as possible [Vicent & Soille, 1991]. The advantage of this technique is that totally closed contours are obtained, and a complete partition of the domain of image is achieved. With this method is not necessary to carry out an additional connection of the edges. The disadvantage of this method resides in that it produces over-segmentation when the objects (to extract) are not appropriately marked. The following definitions and concepts are important for understanding better this method.

In the following, this work equally considers grayscale images as numerical functions or as topographic reliefs. Let H denote the underlying digital grid, which can be of any type: a square grid in four or eight connectivity, or a hexagonal grid in six connectivity. H is a subset of $Z^2 \times Z^2$.

Definition 2.1.2.1: A path P of length l between two pixels p and q in image I is a *(l+1)*-tuple of pixels $(p_0, p_1, \ldots, p_{l-1}, p_l)$ such that $p_0 = p$, $p_l = q$, and $\forall i \in [1,l], (p_{i-1}, p_i) \in H$

Given the previous definition, it will be denoted $l\,(P)$ as the length of a given path P. Also, it will be denoted $N_H\,(p)$ as the set of the neighbours of a pixel p, with respect to H; $N_H\,(p) = \{\, p' \in Z^2, (p, p') \in H \,\}$.

Definition 2.1.2.2 (Catchment basin, first definition): Let I be a grayscale image. The catchment basin $C\,(M)$ associated with a minimum M is the set of pixels p of D_I such that a water drop falling at p flows down along the relief, following a certain descending path called the downstream of p, and eventually reaches M [Vicent & Soille, 1991]. The lines which separate different catchment basins build what is called the *watersheds* (or *dividing lines*) of I. (see Figure 5).
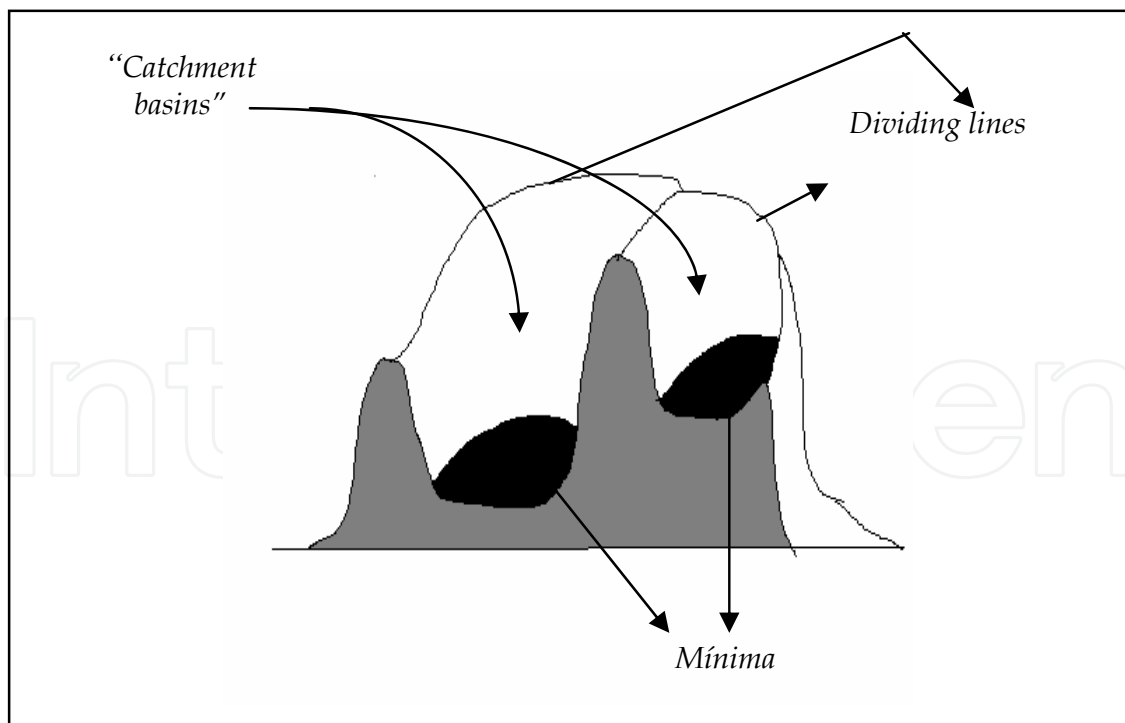

Fig. 5. Minima, catchment basins, and dividing lines

Note that the catchment basins of an image I correspond to the influence zones of its minima, also called areas of attraction of the drops of water. In this sense, it there is a close

relation between the binary skeleton by influence zones and the watersheds. Therefore, this intuitive approach to watershed in not well suited to practical implementations [Vicent & Soille, 1991]. Then, the given definitions in the next section are more suited to the formalization of catchment basins and watersheds in digital space.

Definition 2.1.2.3 (Catchment basin by immersion): Suppose, that in each regional minimum of *I* is pierced a hole, this image being regarded as a topographic surface. Then, this image is slowly immersed into a lake. Starting from the minima of lowest altitude, the water will progressively fill up the different catchment basins of *I*. Now, at each pixel where the water coming from two different minima would merge, a "*dam*" is built (see Figure 6). At the end of this immersion procedure, each minimum is completely surrounded by dams, which delimit its associated catchment basin. The whole set of dams which has been built thus provides a tessellation of *I* in its different catchment basins. These correspond to the dividing lines of *I*.

It is possible to express the immersion procedure more formally [Vicent & Soille, 1991]: *I* being the grayscale image under study, denote h_{min} the smallest values taken by *I* on its domain D_I. Similarly, denote h_{max} the large value by *I* on D_I. In the following, $T_h(I)$ stands for the threshold of *I* at level *h* (see equation (8)). Denote $C(M)$ the catchment basin associated with a minimum *M* and $C_h(M)$ the subset of this catchment basin made of the points having an altitude smaller or equal to *h*:

$$C_h(M) = \{p \in C(M), f(p) \le h\} = C(M) \cap T_h(f) \qquad (10)$$

As concerns the minima of *I*, $min_h(I)$ refers to the set of points belonging to the minima at altitude *h*.
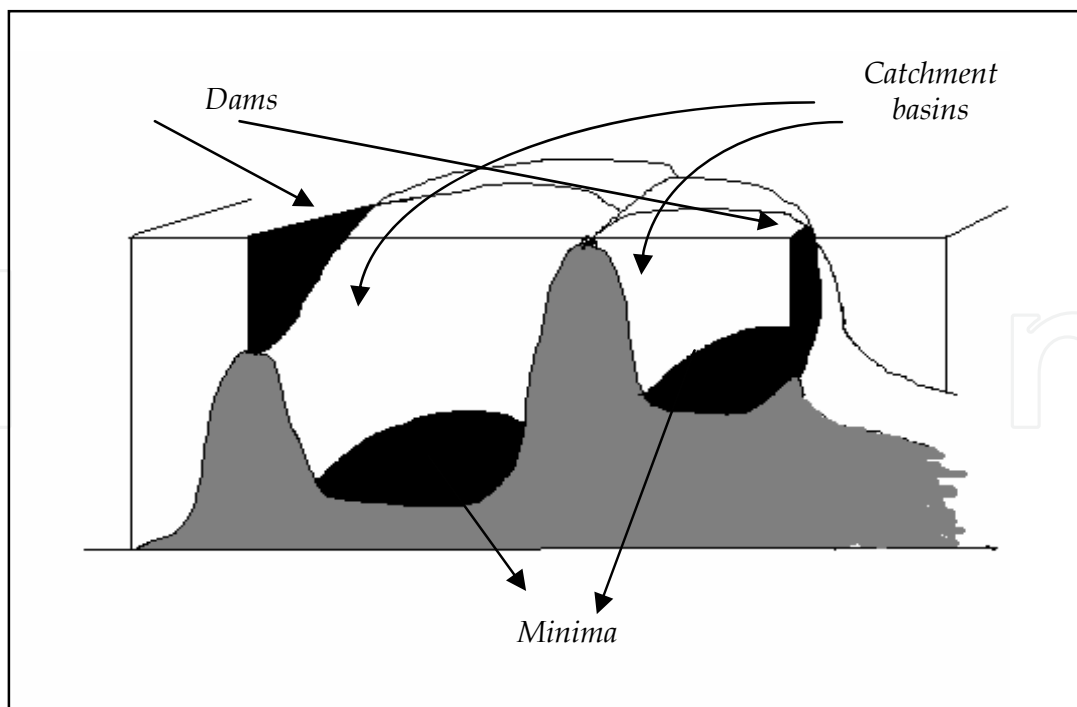

Fig. 6. Building dams at the places where the water coming from two different minima would merge

It is necessary for further understanding in what continues to introduce the definitions of *geodesic distance* and of the *geodesic influence zones*. Let X be a set which is first supposed to be simply connected.

Definition 2.1.2.4: The geodesic distance $d_X (p, q)$ between two pixels p and q in X is the infimum of the length of the paths which join p and q and are totally included in X (see Figure 7):

$$D_X (p, q) = inf \{l (P), P \text{ path between } p \text{ and } q \text{ which is totally included in } X\}$$
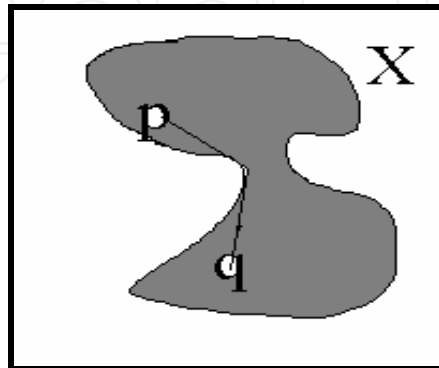

Fig. 7. Geodesic distance between p and q inside X

Suppose that X contains a set B made of several connected components $B_1, B_2, \ldots, B_k$.

Definition 2.1.2.5: The *geodesic influence zone* $iz_X (B_i)$ of a connected component B_i in X is the locus of the points of X whose geodesic distance to B_i is smaller than their geodesic distance to any other component of B (see Figure 8):

$$iz_X(B_i) = \{p \in X, \ \forall j \in [1, k]/ \{i\}, d_X (p, B_i) < d_X (p, B_j) \} \tag{11}$$
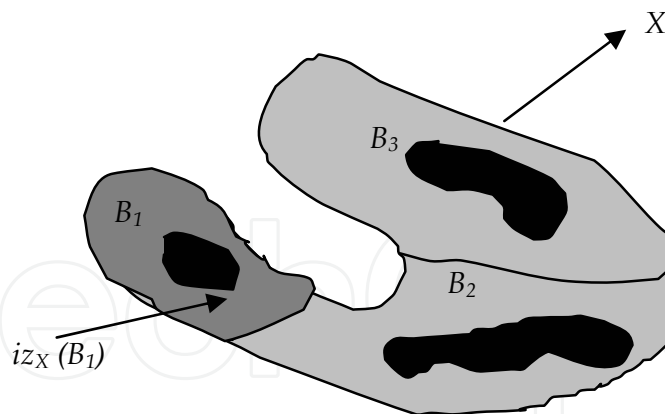

Fig. 8. *Geodesic influence zone* of connected component B_1 inside set X

Those points of X which do not belong to any geodesic influence zone constitute the *skeleton by influence zones, (SKIZ)* of B inside X, denoted $SKIZ_X (B)$:

$$SKIZ_X (B) = X / iz_X (B) \text{ with } iz_X (B) = \bigcup_{i \in [1; k]} iz_x(B_i) \tag{12}$$

In [Vicent & Soille, 1991], it is demonstrated that the previous definitions are easily extended to the case where X is not simply connected, nor even connected at all. Then, finally the following definition is presented.

In order to simulate the immersion procedure, one starts from the set $T_{h_{min}}(I)$, the ponits of which being those first reached by the water. These points constityute the starting set of the recursion. So, of this way,

$$X_{h_{min}} = T_{h_{min}}(I),$$

$X_{h_{min}}$ is made of the points of I which belong to the minima of lowest altitude. For a bigger profundización of the theoretical aspects on this issue see [Vicent & Soille, 1991].

Definition 2.1.2.6 (Catchment basins and Watersheds by immersion): The set of the catchment basins of the grayscale image I is equal to the set $X_{h_{max}}$ obtained after the following recursion:

a) $X_{h_{min}} = T_{h_{min}}(I),$

b) $\forall h \in [\, h_{min}, h_{max} - 1\,], X_{h+1} = min_{h+1} \cup IZ_{T_{h+1}(I)} . (X_h)$

The watersheds transformation of I correspond to the complement of this set in D_I; that is, to the set of the points of D_I which do not belong to any catchment basins. The recursion process between two successive levels is illustrated in Figure 9.
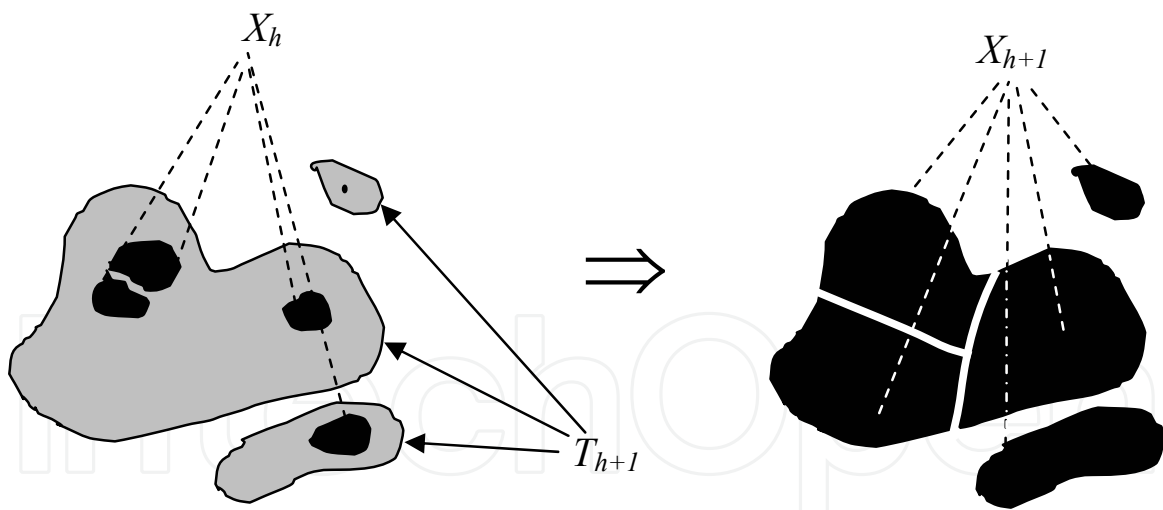

Fig. 9. Recursion process between X_h and X_{h+1}

In many practical cases, one of the principal problems is the obtaining of regional minima, due to the fact that, in general, digital images are corrupted by noise. Then, if one directly applies the watershed transformation to an image many dividing lines are obtained, which is known as over-segmentation.

Therefore, the first step consists in marking the objects we want to segment, and also the background. By marker of an object, it means a connected component of pixels located inside the object to be extracted. To each object one and only one marker must correspond.

The design of robust marker detection techniques involves the use of knowledge specific to the series of images under study. A marking function is then constructed, whose different catchment basins correspond to the desired objects. When one works in the other way, then the watershed transformation produces over-segmentation. The over-segmentation mainly comes from the fact that the markers are not perfectly appropriate to the objects to be contoured. In short, the quality of the segmentation is directly linked to the marking function. If this condition is attained, with the watershed method continuous edges are obtained. With the classical methods this is practically impossible. This statement will be verified in the section corresponding to the experimental results.

The proposed strategy in this work facilitates to obtain a marking function which is of great utility for the watershed segmentation. On one hand, the over-segmentation is avoided and on the other hand, a correct delimitation of contours of the objects of interest is achieved.

2.2 The mean shift and analysis

The iterative procedure to compute the mean shift is introduced as a normalized density estimate of the gradient. By employing a differentiable kernel, an estimate of the density can be defined as the gradient of the kernel density estimate; that is,

$$\hat{\nabla}f(x) = \nabla\hat{f}(x) = \frac{1}{nh^d}\sum_{i=1}^{n}\nabla K\left(\frac{x-x_i}{h}\right)$$

(13)

The function of the kernel $K(x)$ is now a function defined by the vector $\boldsymbol{x}$, d-dimensional, which satisfies

$$\int_{R^d}K(x)dx = 1$$

(14)

Conditions on the kernel $K(x)$ and the window radius h are derived in [Fukunaga & Hostetler, 1975] to guarantee asymptotic unbiasedness, mean-square consistency, and uniform consistency of the estimate in the expression (13). For example, for *Epanechnikov* kernel:

$$K_E(x) = \begin{cases} 1/2c_d^{-1}(d+2)(1-\|x\|^2) & if \; \|x\| < 1 \\ 0 & otherwise \end{cases}$$

(15)

where c_d is the volume of the unit d-dimensional sphere, the density gradient estimate becomes

$$\hat{\nabla}f_E(x) = \frac{1}{n(h^d c_d)}\cdot\frac{d+2}{h^2}\sum_{x_i\in S_h(x)}(x_i-x) = \frac{n_x}{n(h^d c_d)}\cdot\frac{d+2}{h^2}\left(\frac{1}{n_x}\sum_{x_i\in S_h(x)}(x_i-x)\right)$$

(16)

where the region $S_h(x)$ is a hypersphere of radius h having volume $h^d c_d$, centered at $\boldsymbol{x}$, and containing n_x data points; that is, the uniform kernel. In addition, in this case $d = 3$, due to that the vector $\boldsymbol{x}$ has three dimensions, two for the spatial domain and one for the range domain (levels of gray).The last factor in expression (16) is called the *sample mean shift*,

$$M_{h,U}(x) = \frac{1}{n_x} \sum_{x_i \in S_h(x)} (x_i - x) = \frac{1}{n_x} \sum_{x_i \in S_h(x)} x_i - x \qquad (17)$$

The quantity $\dfrac{n_x}{n\,(h^d c_d)}$ is the kernel density estimate $\hat{f}_U(x)$ (the uniform kernel) computed

with the hypersphere $S_h(x)$, and thus we can write the expression (16) as:

$$\hat{\nabla} f_E(x) = \hat{f}_U(x) \cdot \frac{d+2}{h^2} M_{h,U}(x) \qquad (18)$$

which yields,

$$M_{h,U}(x) = \frac{h^2}{d+2} \frac{\hat{\nabla} f_E(x)}{\hat{f}_U(x)} \qquad (19)$$

Expression (19) shows that an estimate of the normalized gradient can be obtained by computing the sample mean shift in a uniform kernel centered on x. In addition, the mean shift has the direction of the gradient of the density estimate at x when this estimate is obtained with the *Epanechnikov* kernel. Since the mean shift vector always points towards the direction of the maximum increase in the density, it can define a path leading to a local density maximum; that is, to a mode of the density (see Figure 10).

In addition, expression (19) shows that the mean is shifted towards the region in which the majority of the points reside. Since the mean shift is proportional to the local gradient estimate, it can define a path leading to a stationary point of the estimated density, where these stationary points are the modes. Moreover, the normalized gradient in expression (19) introduces a desirable adaptive behavior, since the mean shift step is large for low density regions corresponding to valleys, and decreases as x approaches a mode.

Mathematically speaking, this is justified since $\dfrac{\hat{\nabla} f_E(x)}{\hat{f}_U(x)} > \hat{\nabla} f_E(x)$. Thus, the corresponding

step size for the same gradient will be greater than the nearer mode. This will allow observations far from the mode or near a local minimum to move towards the mode faster than using $\hat{\nabla} f_E(x)$ alone.

In [Comaniciu, 2000], it was proven that the mean shift procedure obtained by successive:

- computation of the mean shift vector $M_h(x)$
- translation of the window $S_h(x)$ by $M_h(x)$,

is guaranteed to converge.

A digital image can be represented as a two-dimensional array of *p*-dimensional vectors (pixels), where *p = 1* in the gray level case, *p = 3* for color images, and *p > 3* in the multispectral case.

As was pointed out in [Comaniciu, 2000] when the location and range vectors are concatenated in the joint spatial-range domain of dimension *d = p+2*, their different nature has to be compensated by proper normalization of parameters h_s and h_r. Thus, the multi-variable kernel is defined as the product of two radially symmetric kernels and the Euclidean metric allows a single bandwidth for each domain, that is:
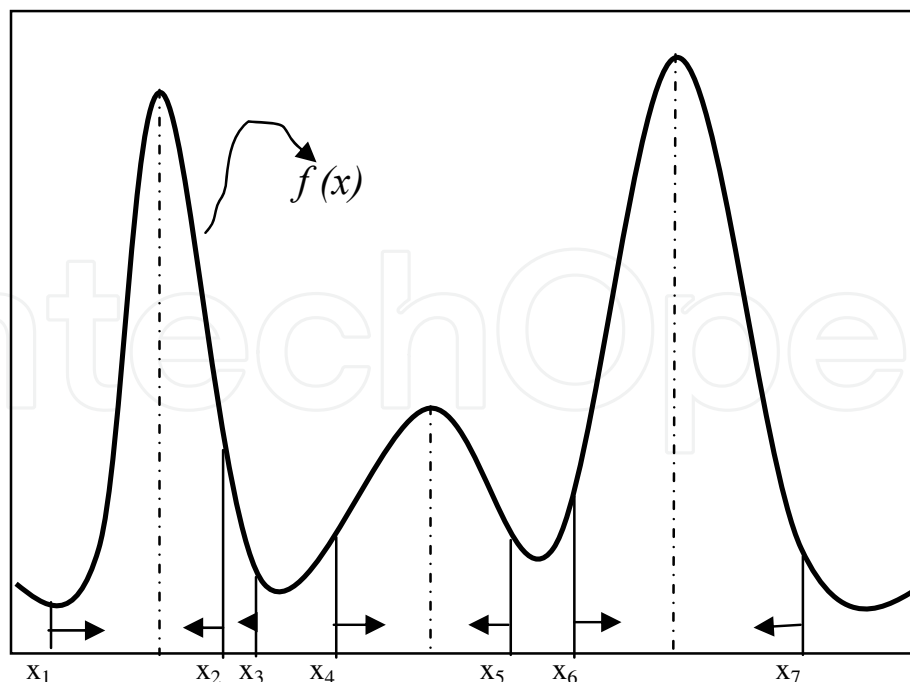
Fig. 10. Gradient mode clustering

$$K_{h_s, h_r}(x) = \frac{C}{h_s^2 \, h_r^p} k\left(\left\|\frac{x^s}{h_s}\right\|^2\right) k\left(\left\|\frac{x^r}{h_r}\right\|^2\right)$$

where x^s is the spatial part, x^r is the range part of a feature vector, $k(x)$ the common profile used in both domains, h_s and h_r the employed kernel bandwidths, and C the corresponding normalization constant. The value hs is associated with spatial resolution of the analysis, while the value hr is associated with the resolution in the domain of range (levels of gray). More details related with the mean shift can be found in [Comaniciu, 2000; Comaniciu & Meer, 2002].

3. Some characteristics of the images under study

Studied images are of arteries, which have atherosclerotic lesions and these were obtained from different parts of the human body, from more of 80 autopsies. These arteries were contrasted with a special tint in order to accentuate the different lesions in arteries. Later, the lesions are manually classified by the pathologists according to World Health Organization. They classified the lesions in type I, II, III and IV. For example, the lesions I and II, these are the fatty streaks and fibrous plaques respectively, while the lesions III and IV are respectively the complicated and calcified plaques. The pathologists mark only the lesions; that is, they do not outline to them. For that reason, the edge automatically detection, it is very important, because these images will be subject to an additional morphometrical analysis in order to study the atherosclerosis and its organic-consequences.

The arteries were directly digitalized from the working desk by using a video camera and an A/D converter. In Figure 11(a) a typical image with lesions I and II can be seen, while in Figure 11(b) is shown its histogram. These images were captured via the MADIP system

with a resolution of 512x512x8 bit/pixels. MADIP- Morphometrical Analysis by Digital Image Processing is a system created to help physicians in his research work using images. MADIP is a software for the morphometrical characterization of macro and micro lesions in biomedical images. In general, it may be used in any branch of science and technology, where not only quantitative techniques of high precision are required, but it is also necessary to do a big number of measurements with high accuracy and rapidly [Rodríguez et al., 2001].

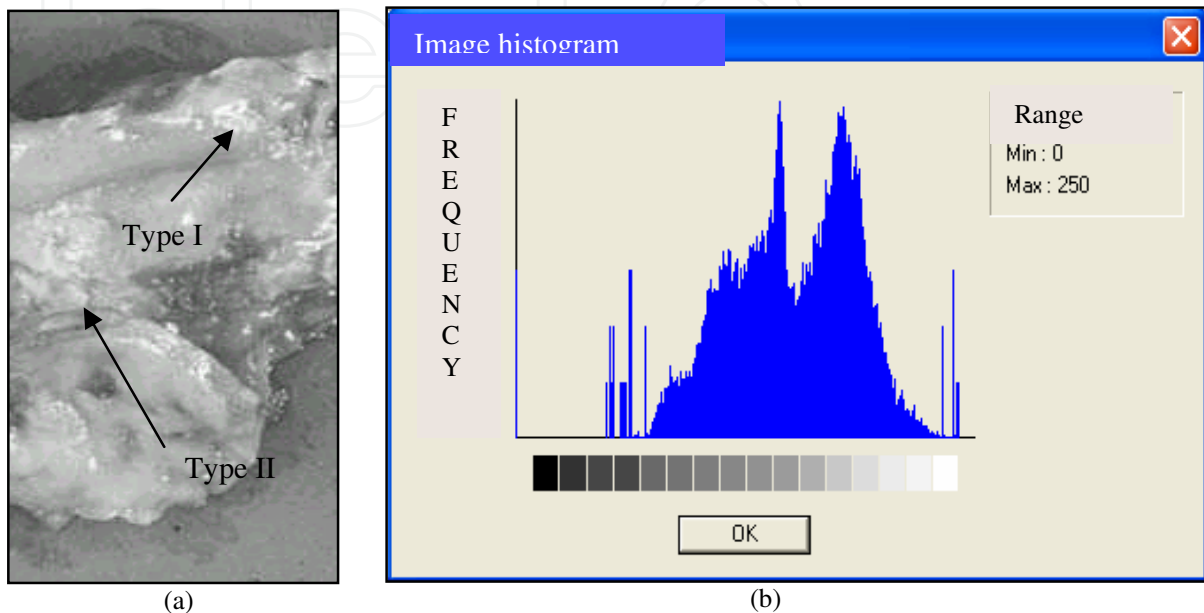(a)   (b)

Fig. 11. (a) Atherosclerosis image. (b) Histogram. It can be observed low contrast. The arrows show an example of structures that we attempt to segment.

Figure 12 shows other examples with other types of lesions.

Fig. 12. Atherosclerosis images with different lesions, which are marked with arrows. The arrows show the lesions.

There are several remarkable characteristics of these images, which are common to typical images that we encounter in the atherosclerotic lesions:
1. High local variation of intensity is observed both, within the atherosclerotic lesions and the background. However, the local variation of intensities is higher within the lesions than in background regions.

2. The histogram of Fig. 11(b) shows that there is a low contrast in the images.
3. The lesions III and IV have better contrast than the lesions I and II (see Fig. 12). In addition, due to variations in the intensity of the background across the image and the low contrast between lesions and background intensities, principally for the lesions I and II, the atherosclerotic lesions in a region of the image may appear lighter than the background in a distant region.
4. It is common of these images the diversity in shape and size of the atherosclerotic lesions.
5. The boundaries of the atherosclerotic lesions, principally for the lesions I and II, may be extremely difficult to define. Due to variations in intensity, both within the lesions and in the background, portions of the atherosclerotic lesion may appear blended into the background, without creating a distinct boundary.

While the characteristics presented above testify the difficulty in identifying atherosclerotic lesions, a close examination reveals information that can be used. We observed that two features of the image, local variation of intensity and image intensity level, can be used to identify regions of the image that describe lesions. High local variation of intensity is exhibited by regions within and near the boundaries of lesions. Thus, local variation of intensity can roughly identify regions of the image that contain lesions. Across the entire image, changes in intensity level cannot reliably distinguish atherosclerotic lesions, due to possible nonuniformity of the average background intensity and low contrast between lesions and background; principally, in the lesions I and II. However, within a region of interest, changes in intensity level can effectively distinguish a lesion, since locally a lesion has major variation of intensities than its surrounding background. The exact shape and size of this region are not important, and hence the region is referred to as an approximate region. Other details on this study can be found in [Rodríguez & Pacheco, 2007].

For the study with images of blood vessels were used biopsies, which represent an angiogenesis process in malignant tumors. These were included in paraffin by using the inmunohistoquimic technique with the complex method of avidina biotina. Finally, monoclonal CD34 was contrasted with green methyl to accentuate formation of new blood vessels. These biopsies were obtained from soft parts of human bodies. This analysis was carried out for more than 100 patients. In Figure 13 can be seen typical images, which were captured via MADIP system with a resolution of 512x512x8 bit/pixels.
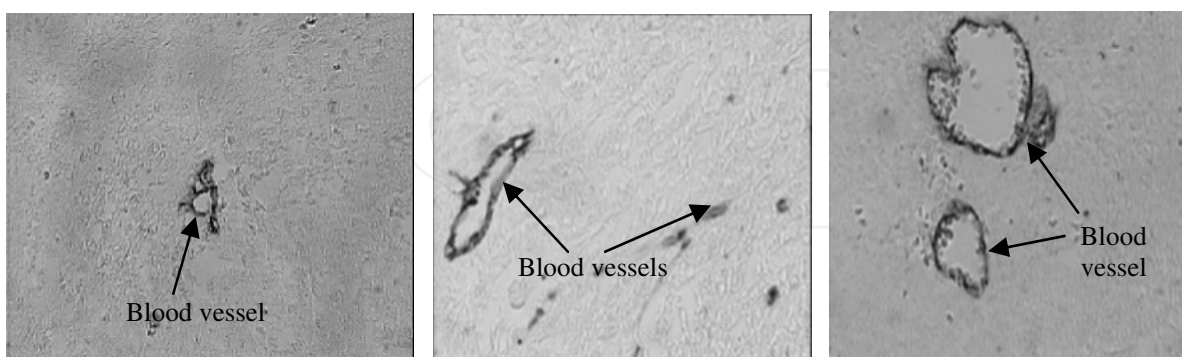

Fig. 13. These images represent the angiogenesis process. The blood vessels are marked with arrows

In Figure 14 a horizontal profile can be observed through the centre of a vessel; that is, a plot of the pixel intensities along a single row. In Figure 15 (b), the histogram of this image is represented.
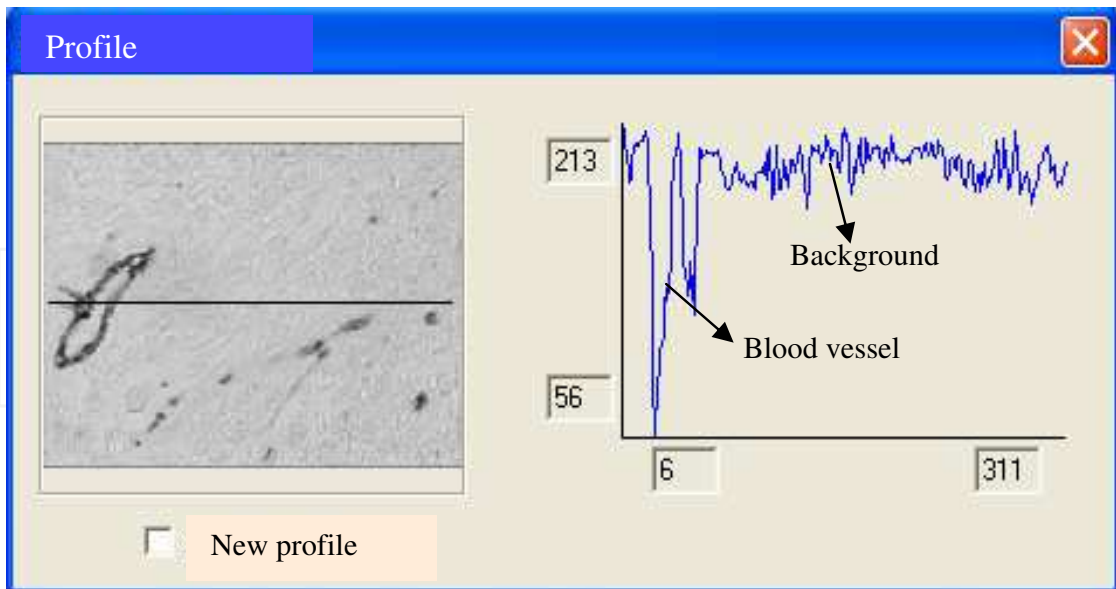
Fig. 14. An intensity profile through the centre of a vessel. Profile is indicated by a line
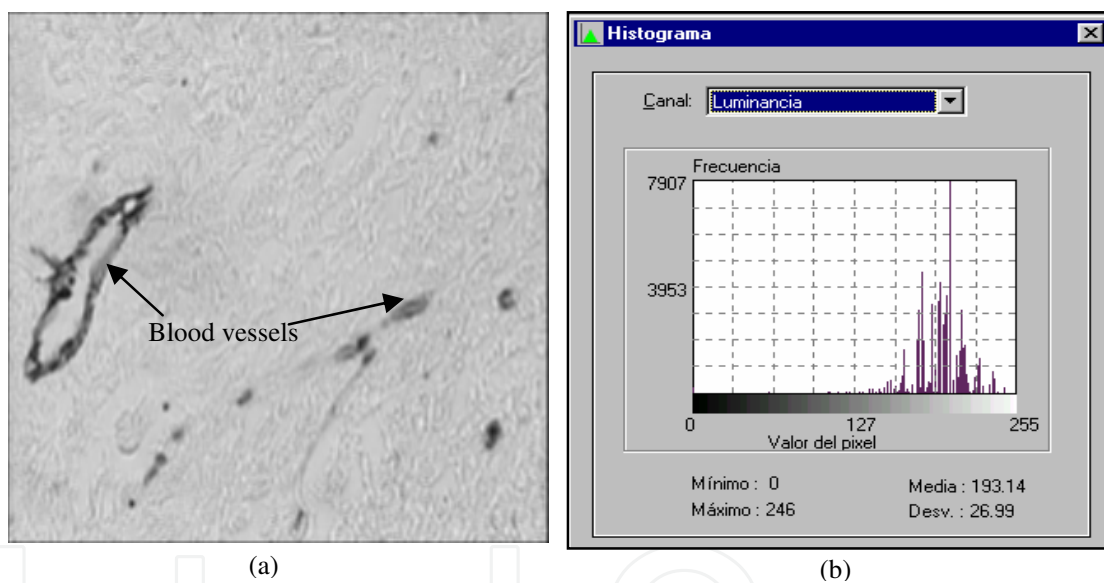

Fig. 15. (a) Original image. (b) Histogram image

There are several notable characteristics of this image, which are common to typical images that we encounter in the tissues of biopsies:

1. The intensity is slightly darker within the blood vessel than in the local surrounding background. It is emphasized that this observation holds only within the local surroundings.
2. High local variation of intensity is observed both within the blood vessel and the background. However, the local variation of intensity is higher within the blood vessel than in background regions (see Fig. 14)
3. The variability of blood vessels both, in size and shape, it can be observed (see Fig. 13).
4. The contrast of intensities between the blood vessel (BV) and the background is low. This is evident from the intensity histogram (see Fig. 15 (b)). This histogram is uni-modal, reflecting the low separation in average intensity of the BV and background.

Due to acquisition protocol, the images are corrupted with a lot of noise. It can be observed the ripple of the histogram in Figure 15(b). Other details on this research can be found in [Rodríguez & Pacheco, 2005].

4. Experimental results and discussion

One of the most important diseases to study is the atherosclerosis and its organic-consequences, which is one of the principal causes of death in the world [Fernández-Britto et al., 1988; Fernández-Britto & Carlevaro, 1989]. The atherosclerosis produces as final consequence the loss of elasticity and increase of the wall of arteries. For example, heart attack, cerebral attack and ischemia are some of its principal consequences [Cotran, 2002]. Strategies that can isolate atherosclerotic lesions in an automatic way constitute important tools for pathologists.

With the goal of diminishing the noise existing in the atherosclerosis images, we used the Gauss filter according to the parameters described in [Rodríguez & Pacheco, 2007]. Figure 16 shows two examples.
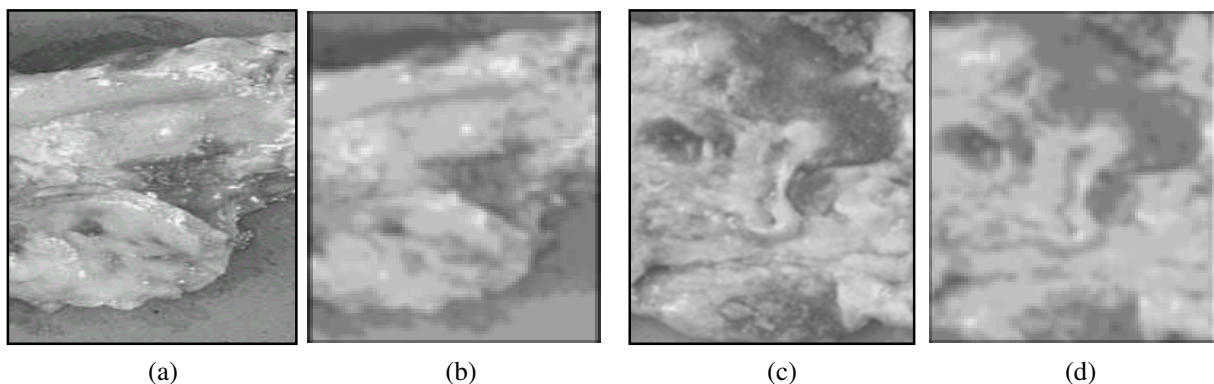

| (a) | (b) | (c) | (d) |

Fig. 16. (a) and (c) Original images, (b) and (d) Filtered images with Gauss ($\sigma = 3$, $5x5$ window size).

One can observe in Figure 16 (b, d) that the images are smoother. It is possible to see that the atherosclerotic lesions are more uniform, which is indicative that the noise was diminished.

In a second step, we carried out a modification of the histogram to these images, according to the algorithm presented in [Rodríguez & Pacheco, 2007]. This procedure was carried out in order to increase the contrast. We show in Figure 17 the obtained results.

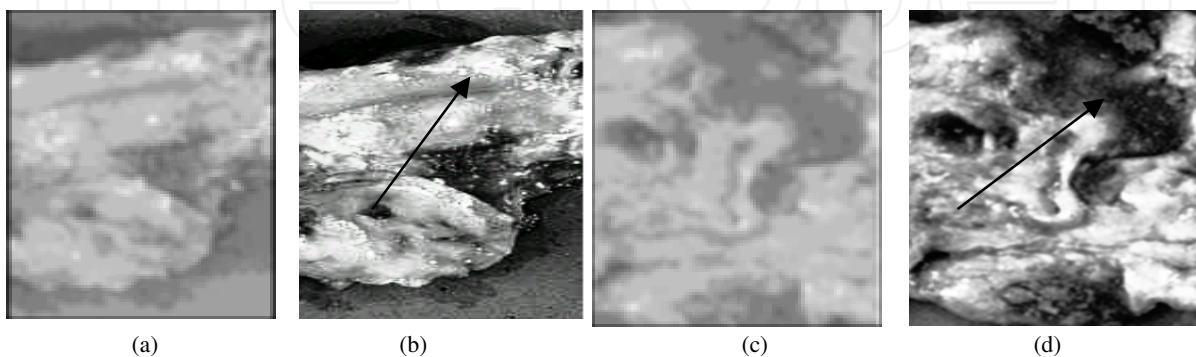| (a) | (b) | (c) | (d) |

Fig. 17. (a) and (c) Filtered images with Gauss. Figures (b) and (d) contrasted images. It is evident the good obtained result with the enhancement.

We shall carry out a general description of the proposed method before going into the details of each one of the steps, which will allow having a panoramic vision of the proposed solution. In Figure 18 is depicted all steps of the proposed strategy to obtain robust markers for the atherosclerotic lesions.
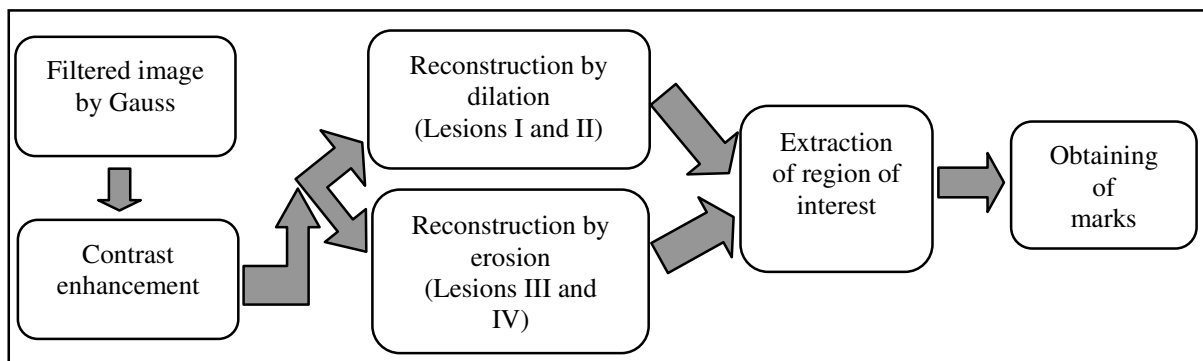

Fig. 18. Steps to obtain the markers of atherosclerotic lesions

It is very important to point out that the proposed strategy was obtained according to experimentation; that is, we carried out firstly a morphological reconstruction by erosion for all lesions (see definition 2.1.4), and secondly, we carried out a morphological reconstruction by dilation for all lesions (see definition 2.1.2). We verified that, in all cases for the lesions I and II, the best results by using a reconstruction by dilation were obtained; while for the lesions III and IV the best results were obtained carrying out a reconstruction by erosion. This affirmation will be appreciated in the next steps. We processed 100 images in total, but for space problem, we only reported 10 cases.

In order to cope with problems previously cited and with the goal of extracting the approximate regions of interest; after the histogram modification, we carried out a morphological reconstruction. The region of interest is a region that contains the lesion and its neighboring background, where the exact shape and size of this region are not important. This region of interest is referred to an approximate region. We verified that the reconstruction by erosion (for the lesions III and IV) led to an image where the dark zones correspond to these lesions. For example, in Figure 19 is shown the obtained result for a lesion of type IV.
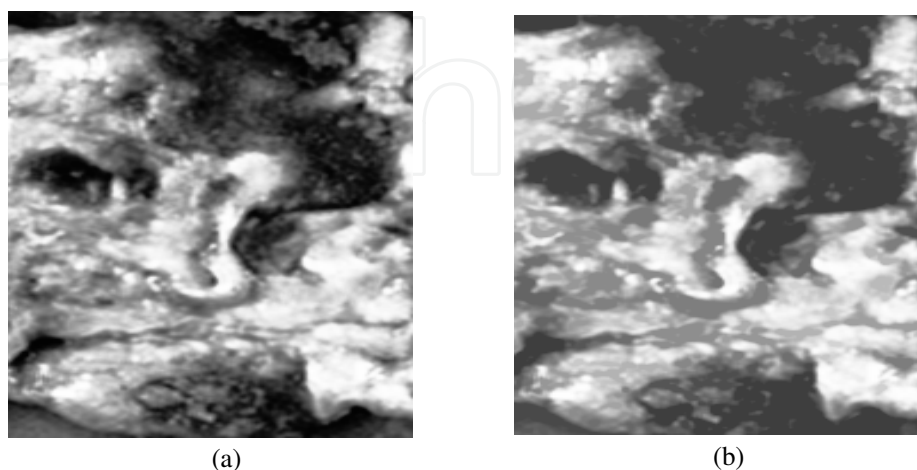

(a) (b)

Fig. 19. (a) Resulting image of the histogram modification. (b) Image obtained by a reconstruction by erosion. The dark parts correspond to the lesion IV.

The result in Figure 19(b) was obtained by using a rhombus as structuring element of *5x5* pixels and a height equal to *60* (see definition 2.1.1.3). Basically,   we used   the *h*-domes, where the principle is to subtract an arbitrary constant *h* from the original image *I* and to perform a grayscale geodesic reconstruction of *I* from *I+h* (*J = I+h)*. This provides a useful technique for extracting "*domes*" of a given height *h*. The choice of *h* turns out not to be a critical operation, since a range of values yield correct results, which we verified in the practice. In addition, the selection of this structuring element and its size was obtained via experimentation. It is important to point out that when one speaks of size of the structuring element its dimension is in pixels. In addition, the structuring element is plane. For an understanding better on this aspect, as an example, the form and size of four structuring elements are shown (see Figure 20).

In Figure 21, it is represented the obtained results (in the reconstruction) for other structuring elements. In all cases in order to carry out the geodesic reconstruction, the considered height was equal to *60*.

As can be appreciated in Figure 21(a), for a structuring element minor than *5x5* pixels, the area of the atherosclerotic lesions decreased. Comparing the image of Figure 19 (b) with those of Figures 21(b) and 21(c), one can see that for structuring elements (rhombus or circle) major than *5x5* pixels, the obtained results were very similar, but the computation time was increased. In Figures 21(d), 21(e) and 21(f), it can be observed that for diagonal segments as structuring elements, the obtained results were not good. The lesions were notably deformed. For these reasons, we considered that the rhombus of *5x5* pixels was the most suitable. This behaviour was similar for the 100 processed images.

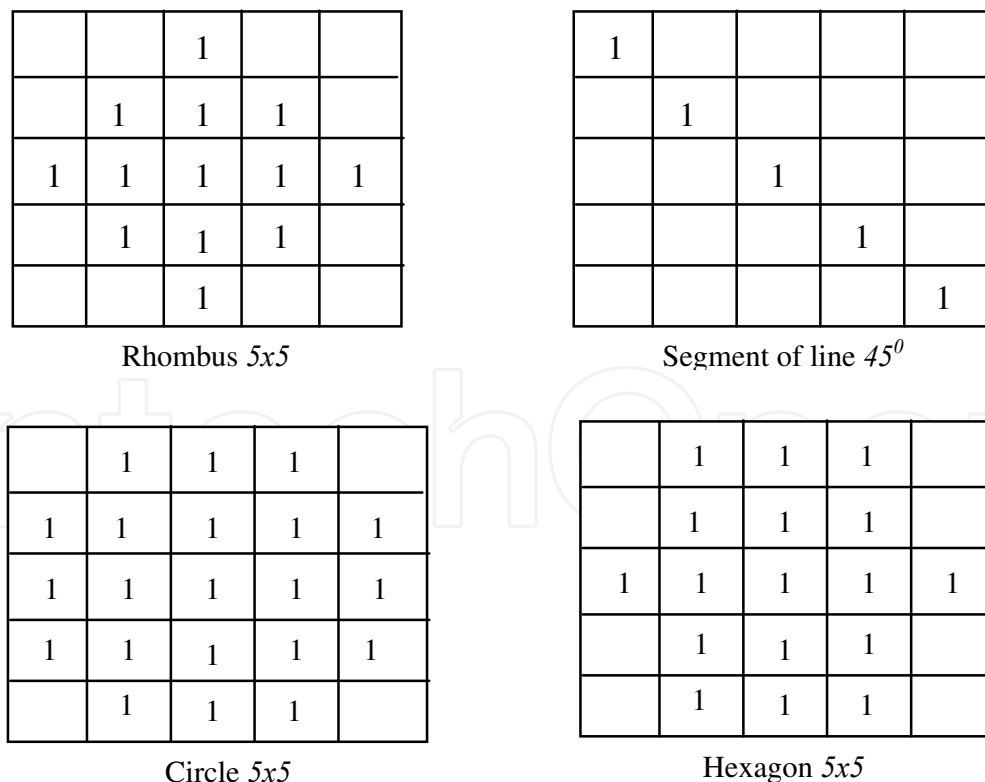|		1		
	1	1	1	
1	1	1	1	1
	1	1	1	
		1		

Rhombus *5x5*

1				
	1			
		1		
			1	
				1

Segment of line *45⁰*

	1	1	1	
1	1	1	1	1
1	1	1	1	1
1	1	1	1	1
	1	1	1	

Circle *5x5*

	1	1	1	
	1	1	1	
1	1	1	1	1
	1	1	1	
	1	1	1	

Hexagon *5x5*

Fig. 20. Four structuring elements; superior left: rhombus of size *5x5* pixels, superior right: diagonal segment of *5* pixels, inferior left: circle of *5x5* pixels and inferior right: hexagon of *5x5* pixels.

With respect to the height for carrying out the geodesic reconstruction, we verified that for all our images the optimal values were in the range from *40* to *60*. In fact, in Figure 22 are depicted the obtained results considering a height out of this range.

In Figures 22 (b) and 22 (c), one can observe that for a large height the atherosclerotic lesions were very smoothed. Furthermore, the areas of the lesions also were increased. Some of them were fused (see arrows). For a height smaller than *40*, according to the criterion of pathologists, the area of the atherosclerotic lesions decreased (see Fig. 22(a)). Then, in these cases, an exact delimitation of the lesions is not obtained and the final results will be poor. This behavior was similar for all the processed images, which is not included here by space problem.
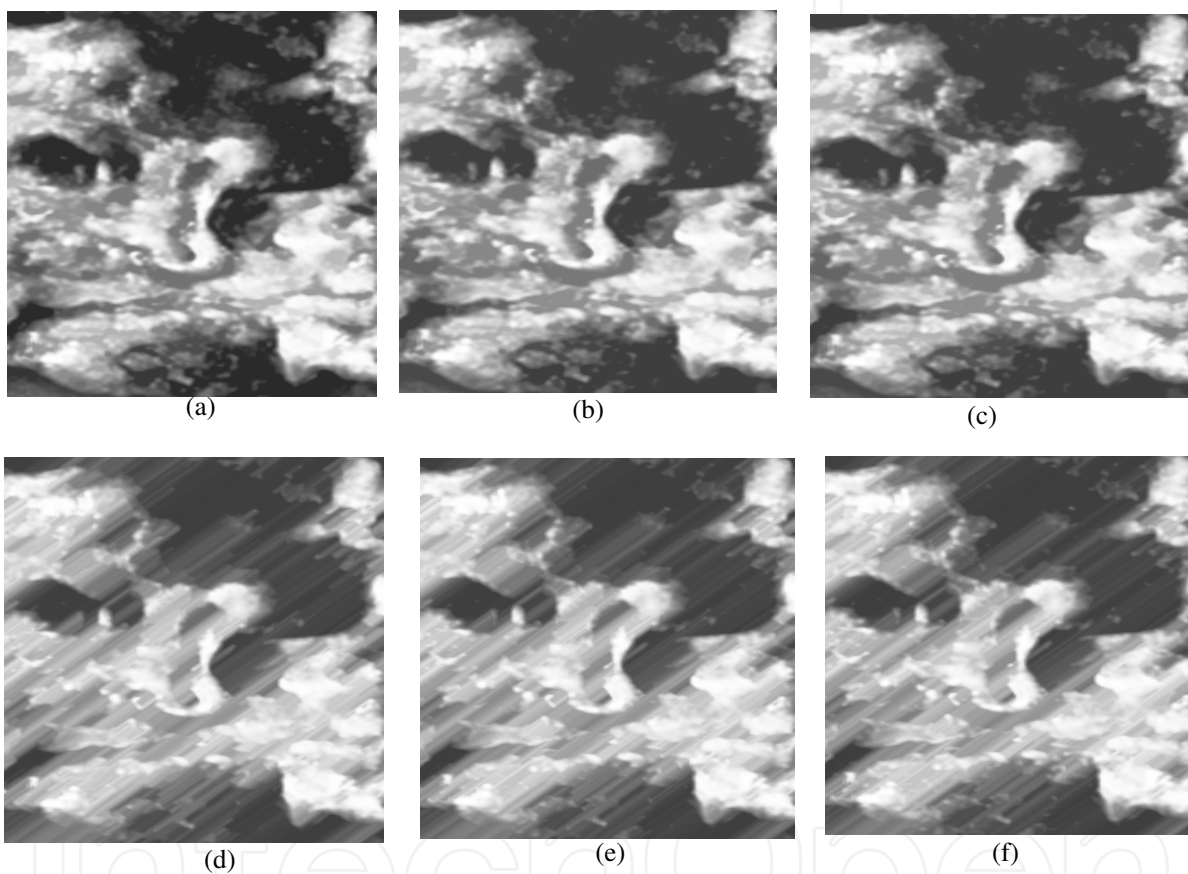

(a)   (b)   (c)

(d)   (e)   (f)

Fig. 21. (a) Reconstruction by a rhombus of *3x3* pixels. (b) Reconstruction by a rhombus of *7x7* pixels. (c) Reconstruction by a circle of *7x7* pixels. (d) Reconstruction by a diagonal segment (45^0) of *3* pixels. (e) Reconstruction by a diagonal segment of *5* pixels *(45^0)*. (f) Reconstruction by a diagonal segment of *7* pixels *(45^0)*. The height was equal to *60*.

After obtaining both, the size of structuring element and the optimal height, the next step of our strategy was to segment the approximate region of interest. That is, as it was pointed out, a region that contains the atherosclerotic lesion and its neighbouring background. This step was carried out by applying a simple threshold through Otsu method [Otsu, 1978]. The thresholding value does not have much influence on the performance, because the exact shape and size of this region are not important. In this case, the region is referred to as an approximate region. In Figure 23(b) one can see the region of interest.
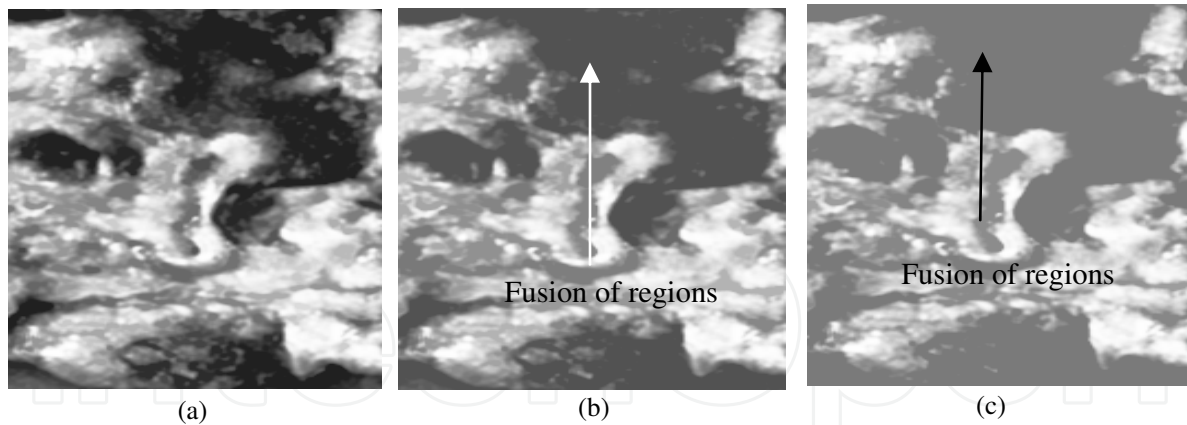
(a)   (b)   (c)

Fig. 22. (a) Reconstruction with a rhombus of *5x5* and height equal to *30*. (b) Reconstruction with a rhombus of *5x5* and height equal to *80*. (c) Reconstruction with a rhombus of *5x5* and height equal to *120*.
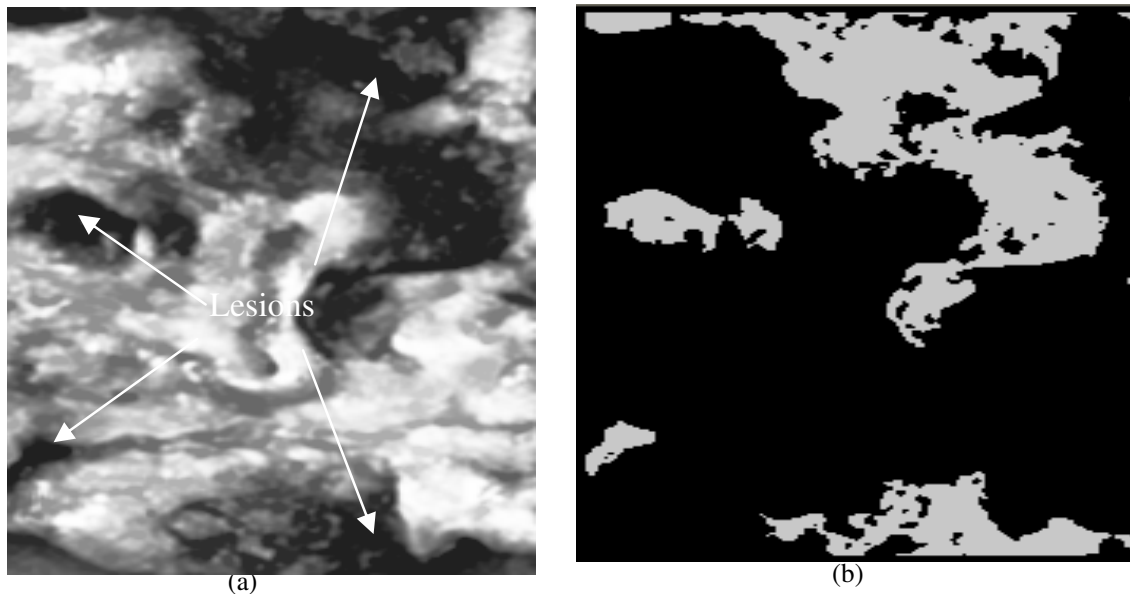

(a)   (b)

Fig. 23. (a) Image of the reconstruction, where the arrows indicate the lesions. (b) Regions of interest

In Figure 23 (b), it is possible to observe that all the indicated lesions in Figure 23 (a) were detected. Furthermore, it can be seen that the regions of interest don't have the exact size of the lesions, since they simply are an approximation. We verified that the regions of interest, in general, were smaller than the atherosclerotic lesions. This result was the same one for all the processed images. Other regions of interest will be able to be observed in the next section. After this result, we developed an algorithm to obtain markers for the atherosclerotic lesion.

4.1 Algorithm to obtain markers
The steps of the algorithm are described below:
1. *Obtain the regions of interest, which as we pointed out, it are those regions belonging to the lesions and they are obtained through a thresholding procedure, after carrying out the*

geodesic reconstruction. To the resulting image of this procedure we will call IREZI.

2. *Label the resulting image of the step 1. This step is as follows. Create an auxiliary image with all pixels in zero: Let IA1 be this image. Scan IREZI at iterative way, then in this image all the background is labeled with a value equal to 1.*

3. *With the goal of finding connected components, scan IREZI again from the top to the bottom and from the left to the right. If there is a pixel, which belongs to a connected component and in the image IA1 this pixel has zero value, then other iterative method begins to work. This new iterative method marks with a determined value within the image IA1 all pixels belonging to a connected component. In addition, pixels within the image IREZI are also marked with a value, which identifies the connected component to which they belong. This action is carried out in the whole image. As this step is finished, in the image IREZI all the connected components were filled and in the image IA1 all the connected components were labeled.*

4. *Create other auxiliary image (let IA2 be this image) with the same values of the image IA1. Also create an array, which controls if a connected component was reduced. In the image IA2 is where in each step the reduction of the connected components are obtained, the final result is represented in the image IA1.*

5. *Scan the labeled image (IA1). When in this image a pixel is found, which belongs to a connected component, through other iterative method, this component is reduced and in the image IA2 all the frontiers of the connected component are marked. If still there is some pixel within the connected component, which is no frontier, in the images IA2 and IA1, the mentioned pixel is eliminated and this function begins again until that all points are frontiers. In this case, the obtained result (reduction) is taken as the mark. In the array (see step 4) it is indicated that the labeled component with this value was processed and it is began to look for other component.*

6. *Finish when the image IA1 is completely scanned. When this step is concluded, in the image IA1 all marks of the atherosclerotic lesions are. These marks are collocated in the image IREZI. Here, after the step two, the connected components (in IREZI) were filled. The image IREZI is the resulting image.*

All the functions in *C* of this algorithm appear in [Rodríguez & Pacheco, 2007]. The result of carrying out this algorithm to the image of Figure 23(b) is shown in Figure 24. In Figure 24(b) one can see that the mark is unique for each of the lesions, which is always inside the atherosclerotic lesion. In this case, we firstly applied this algorithm to the regions of interest of the lesions III and IV. In other words, to the contrasted images of this type of lesions (III and IV) a reconstruction by erosion is carried out, later we applied a thresholding in order to obtain the regions of interest; lastly the proposed algorithm is applied to the image of the regions of interest (see Fig. 24 (b)). This procedure is the same one for all the lesions III and IV. In total *40* lesions of type III and IV, it were processed.

Now, we shall explain the steps that we carried out to obtain the marks for the lesions I and II (see Fig. 18). In this case, the first step was to carry out a modification of histogram according to the algorithm that appears in [Rodríguez & Pacheco, 2007]. After this step, we carried out a reconstruction by dilation. This reconstruction improved, even more, the contrast of the lesions I and II. Figure 25 shows the obtained result of the reconstruction.
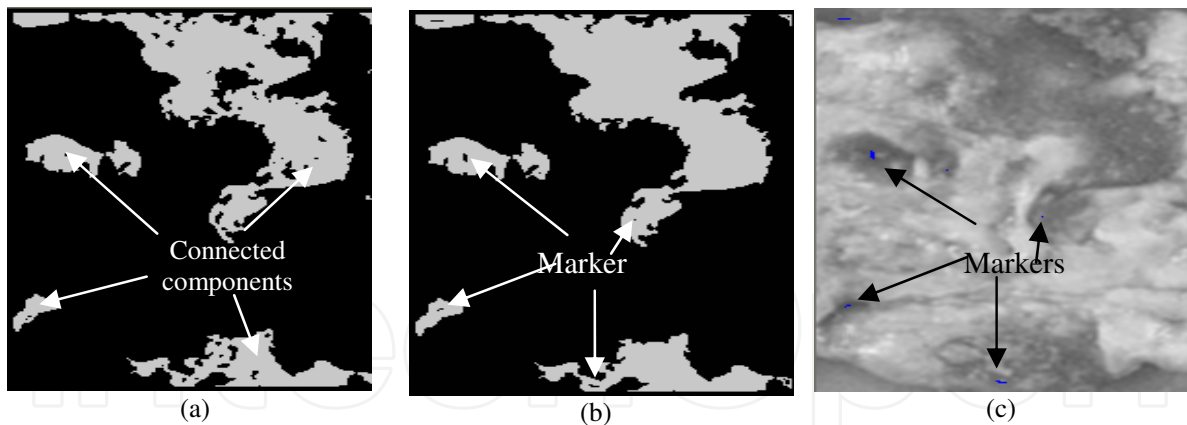
Fig. 24. (a). Image with regions of interest, (b) Marking image, (c) Marks superimposed on the original image
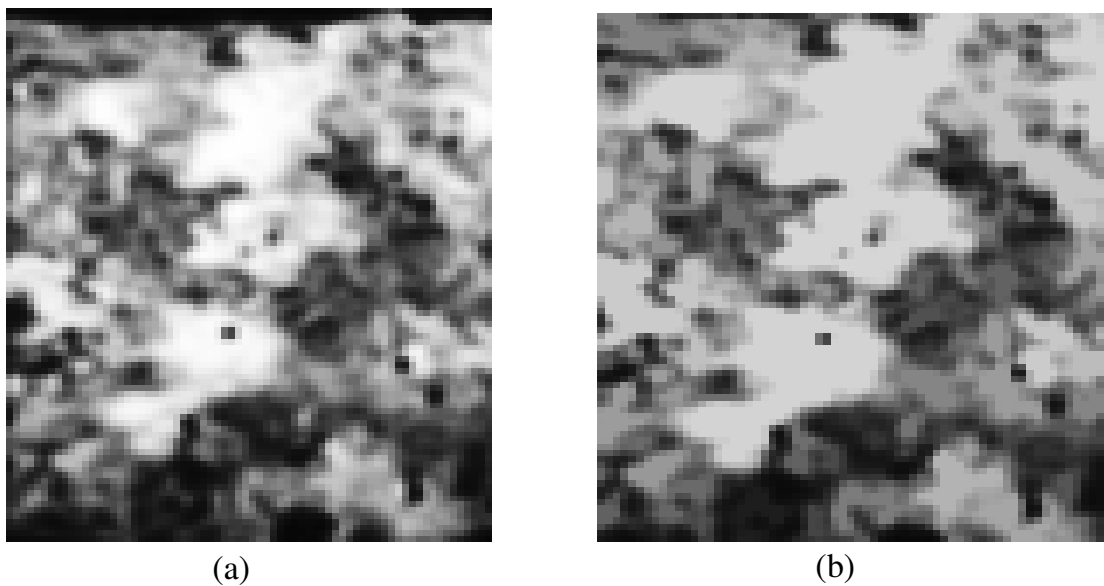

Fig. 25. (a) Initial image. (b) Reconstruction by dilation (lesion II)

The result in Figure 25(b) was obtained by using a structuring element type rhombus of *5x5* pixels, similar to the one used for the lesions III and IV. In this case, the used height in order to carry out a geodesic reconstruction by dilatation was equal to *40*. Also, for these lesions (I and II), several experiments with distinct structuring elements were carried out. The obtained results were very similar to those depicted in Figures 21 and 22. We verified that the structuring element type rhombus of *5x5* pixels was of the best performance. In addition, with respect to height for the reconstruction, we concluded that the optimal height was in the range from *40* to *60* too. Out of this range, similar results were obtained as in the lesions III and IV. This experiment was carried out for a total of 50 images (lesions I and II). All the obtained results were not shown here because they were very similar. Later, we obtained the approximate region of interest via a thresholding and lastly, the markers were obtained through the algorithm presented in section 4.1. The obtained result is shown in Figure 26. One can observe that the regions of interest are not exactly the atherosclerotic lesions, but simply an approximate region.
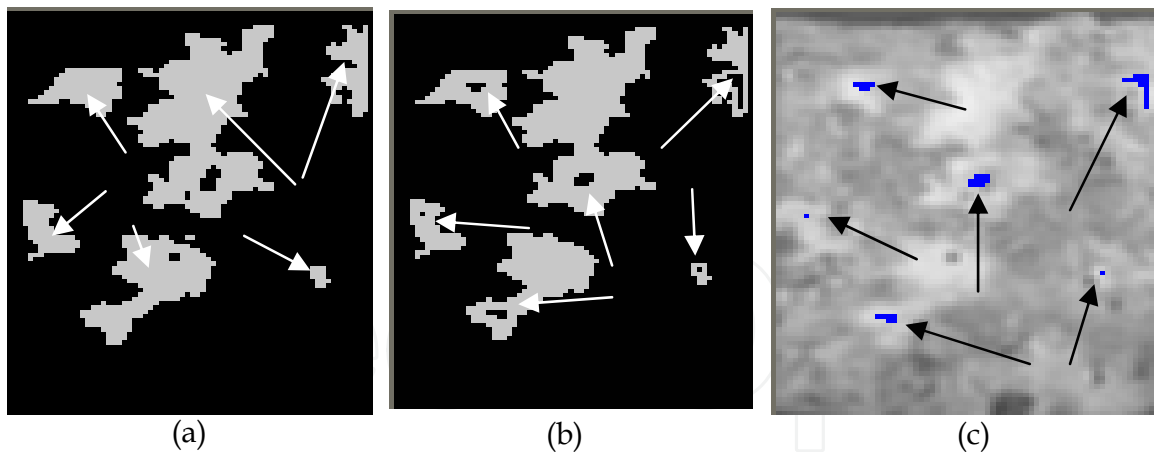
Fig. 26. (a) Regions of interest. The arrows indicate the connected components. (b) Image with marks. (c) The marks superimposed on the original image.

In Figure 26(b) it is possible to see that the marks are unique for each of the lesions, which are always inside the atherosclerotic lesion. This aspect is very important.

4.2 Application of the proposed strategy for atherosclerosis image segmentation by using the watershed method

As have been pointed out the watershed transformation has the drawback of producing over-segmentation. This is true even if one had taken the precaution of filtering the initial image or its gradient. In fact, Figure 27(b) shows the obtained result as we directly applied the watershed transformation to an atherosclerosis image without good markers for the lesions. It is evident as the contours of the atherosclerotic lesions were not well detected and it is observed a lot of noise. However, in Figure 27(c) is shown the excellent obtained result according to our strategy and the introduced algorithm in this work (see section 4.1). The contours of the atherosclerotic lesions were well defined.
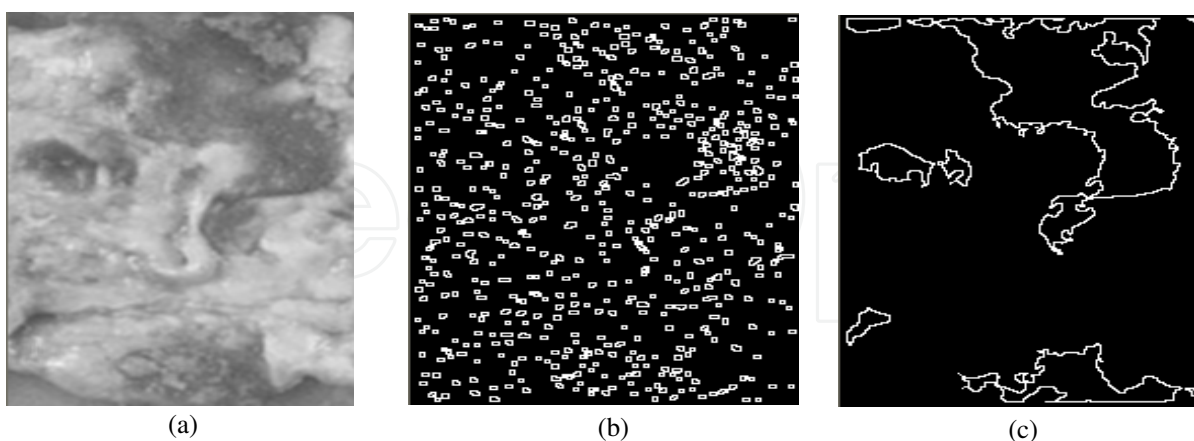

Fig. 27. (a) Original image. (b) The watershed segmentation without marks in the lesions. (c) The watershed segmentation according to our strategy.

In Figure 28, we show the contours superimposed on the original image in order to see the exact coincidence of the obtained contours. This result is evident.
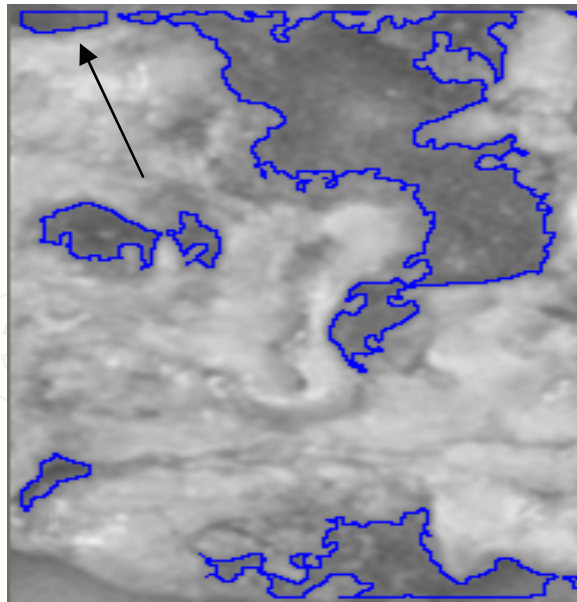
Fig. 28. The contours superimposed on the original image. It is possible to see the exact coincidence of the contours on the lesions. The arrow indicates an object, which does not correspond to an atherosclerotic lesion. In [Rodríguez & Pacheco, 2007], a quantitative evaluation of this algorithm was carried out.

In Figure 29, another example of the application of watershed method on other atherosclerosis image is shown. In Figure 29 (b), we applied watershed segmentation on the gradient of image. It is evident that, even though the watershed method was applied on the gradient of image, an over-segmentation was produced. In Figure 29 (c), one can observe the obtained result of carrying out our strategy. In Figure 30 is shown the obtained contours with our strategy superimposed on the original image. It is possible to observe the exact coincidence of the contours on the lesions.

(a)   (b)   (c)
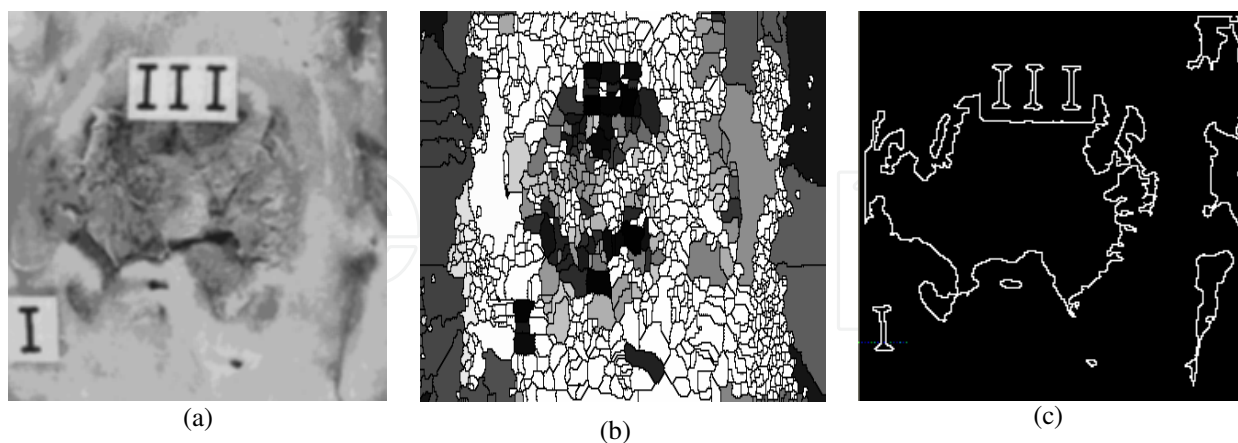
Fig. 29. (a) Original image. (b) Watershed transformation on the gradient of the original image (c) The watershed segmentation according to our strategy.

This same strategy was applied for image segmentation of blood vessels [Rodríguez et al., 2005], but here we will expose the obtained results on these images (blood vessels) by using the mean shift.
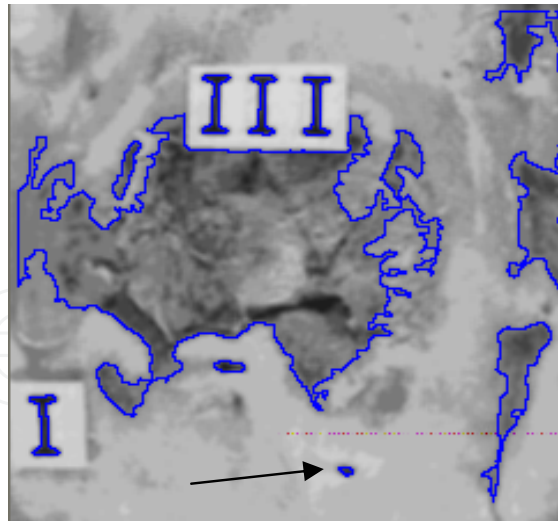
Fig. 30. The contours superimposed on the original image. The arrow indicates an object, which does not correspond to an atherosclerotic lesion (see reference [Rodríguez & Pacheco, 2007])

4.3 Obtained results in image segmentation of blood vessels by using the mean shift

The angiogenesis process is an important aspect in the histopathological research of diseases [Díaz-Flores et al., 1994]. This process is studied by pathological anatomy and it is characterised by a new formation of blood vessels in the tissue, which increases its growing. Angiogenesis is a normal process that occurs in all tissues, but it is known that in pathological cases the increase of blood vessels is abnormal. For example, in mammary, prostate, bladder and brain cancers the greater the number of blood vessels, the more developed the disease is [Díaz-Flores et al., 1994].

In the study of the angiogenesis process the pathologists analyse all information related with the blood vessels by using a microscope. This work is very tedious and time consuming and obviously, the automation of this analysis is highly desirable. In such a sense, a useful task for digital images processing should be the segmentation of blood vessels.

In this work we utilized the mean shift for segmentation of blood vessels. So, we proposed a segmentation algorithm, which will be exposed next.

In general, an image captured with a real physical device is contaminated with noise and in most cases a statistical model of white noise is assumed, mean zero and variance σ. For smoothing or elimination of this form of noise many types of filters have been published, the most classic being the low pass filter. This filter indiscriminately replaces the central pixel in a window by the average or the weighted average of pixels contained therein. The end result with this filtering is a blurred image; since this reduces the noise but also important information is taken away from the edges. However, there are low pass filtering techniques that preserve the discontinuities and reduce abrupt changes near local structures. A diverse number of approaches have been published taking into consideration the use of adaptive filtering. These range from an adaptive Wiener filter, local isotropic smoothing, to an anisotropic filtering. The mean shift works in the spatial-range domain, but differs from it (anisotropic filtering) in the use of local information.

The algorithm that was proposed in [Comaniciu & Meer, 2002] for filtering through mean shift is as follows:

Let $\{x_i\}_i$ and $\{z_i\}_i$, $i = 1,\ldots,n$ be the input and filtered images in the joint spatial-range

domain. For each pixel $p \in x_i, p = (x,y,z) \in \Re^3$, where $(x,y) \in \Re^2$ and $z \in \left[0, 2^B - 1\right]$, B

being the quantity of bits/pixel in the image. The filtering algorithm comprises the
following steps:

> *For each $i = 1,\ldots,n$*
1. *Initialize $j = 1$ and $y_{i,1} = p_i$.*
2. *Compute the mean shift in order to obtain the mode where the pixel converges; that is, the calculation of the mean shift is carried out until convergence, $y = y_{i,c}$.*
3. *Store at Z_i the component of the gray level of calculated value: $Z_i = \left(x_i^s, y_{i,c}^r\right)$, where x_i^s is the spatial component and $y_{i,c}^r$ is the range component.*

4.3.1 Proposed segmentation algorithm via mean shift

*1. Run the mean shift filtering procedure for the image according to former steps, and store all the information about the d-dimensional convergence point in **Zi**.*

2. Define the regions, which are found in the spatial domain (h_s) with intensities smaller or equal than $h_r/2$.

*3. For each region, which was defined in the step 2, look for all the pixels belonging to the region whose mean intensity values are assigned at **Zi**.*

4. Build the region graph through an adjacent list as follows: for each region, look for all adjacent regions to the right or under the region.

5. While there are nodes in the graph, which have been not visited, run a variant of the "Depth-First Search" (DFS), which allows concatenating adjacent regions; as parameter one has to provide a node which has been not yet visited. To do this the next steps are carried out:

> *5.1. Mark the mentioned node as visited.*
> *5.2. While there is children not yet visited:*
> > *children = current child*
> > *if $|Z_{parent} - Z_{child}| < = h_r$, then,*
> > *The region of the child is fused with the region of the father, where the same label is assigned and it is marked as visited.*
> *5.3 To the parent is assigned the children of the visited child from the first position and the children which have been not visited are remained.*
> *5.4 Look for the following child and come back to step 2 while stability it is not obtained (i.e., no more pixel values are modified).*

6. Eliminate spatial regions containing less than M pixels, since those regions are considered irrelevant.

7. (Binary): To all the pixels belonging to background, assign the white color to the objects and the black color to the background.

The effectiveness of this algorithm was recently proven in [Rodríguez et al., 2008]. In that
paper was carried out a comparison of the obtained results with this algorithm and those
attained by using the spectral methods.

Now, some of the obtained results will be exposed, in real images, using the proposed segmentation algorithm of the mean shift. In Figure 31 are presented a first example where one can appreciate the segmentation result.
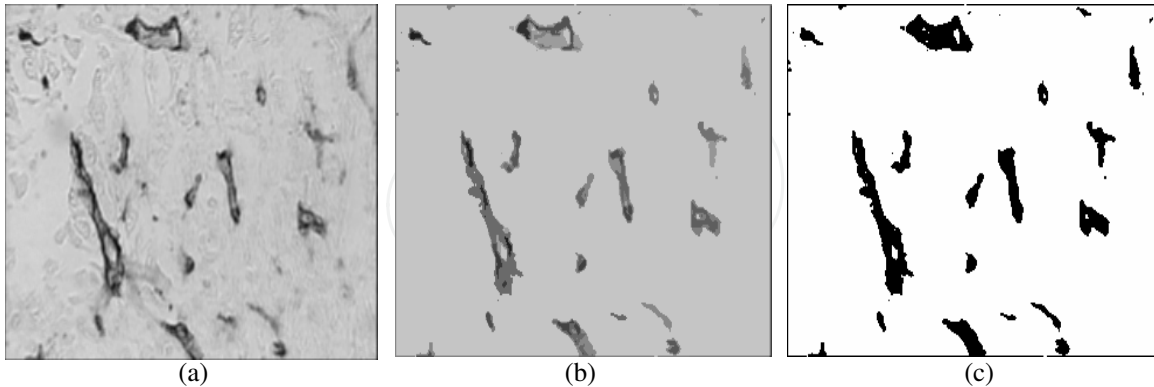

(a) (b) (c)

Fig. 31. (a) Original Image, (b) Image segmented with the proposed algorithm (*hs=4, hr=15, M =20*), (c) Binarized image.

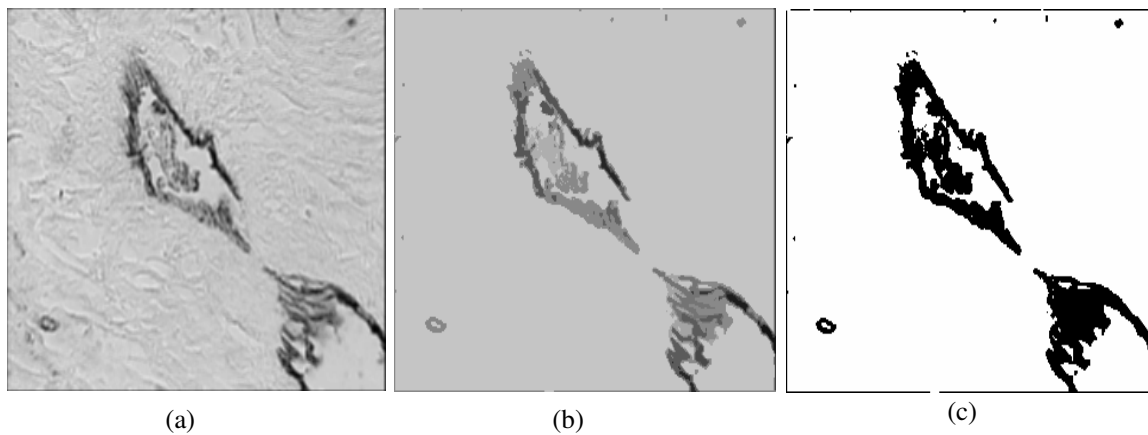In Figures 32 and 33, other two segmentation examples appear using the proposed algorithm.

(a) (b) (c)

Fig. 32. (a) Original Image, (b) Image segmented with the proposed algorithm (*hs=4, hr=15, M =20*), (c) Binarized image.
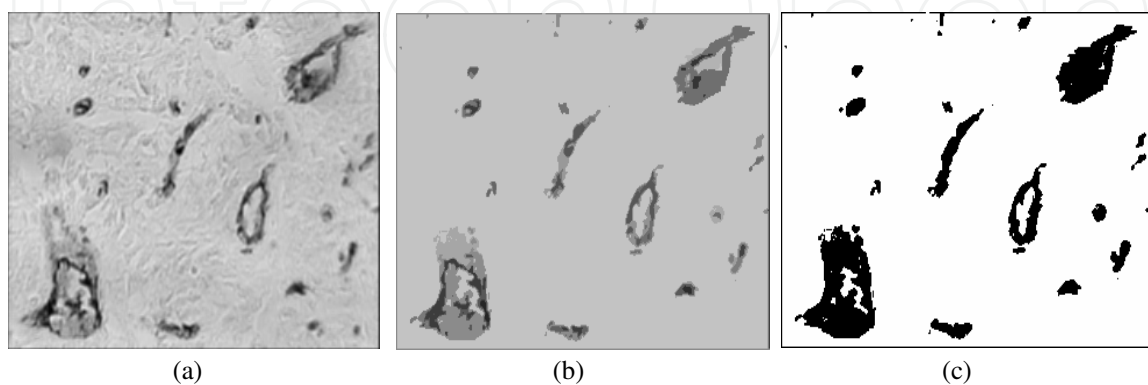

(a) (b) (c)

Fig. 33. (a) Original Image, (b) Image segmented with the proposed algorithm (*hs=4, hr=15, M =20*), (c) Binarized image.

One can see in Figures 31, 32 and 33 the robustness of the obtained results using the proposed segmentation algorithm. According to the opinion of specialists the method was able to discriminate all the objects of interest (blood vessels). This is of supreme importance from the point of view of the diagnosis. It is also observed that the obtained results are free of noise; in addition, for all the segmented images the same parameters h_r and h_s were used.

By the way of examples, two of the obtained results in [Rodriguez et al., 2008] it will be exposed. These results are shown in Figure 34 and 35. In the presented examples, the reader can appreciate that both methods were able to effectively well isolate the blood vessels. However, one also can see that the segmented images via the mean shift algorithm were less noisy than those obtained via the spectral method. Furthermore, the edges were more robust and better defined in the images segmented with the mean shift.

In order to obtain less noisy images with the spectral method it would be necessary to carry out an additional step of filtering with the aim of eliminating the noise that arises during the segmentation process. This procedure could be carried out through a morphological technique, which can be an opening or a majority filter. Another way could be to use the mean shift procedure as a pre-processing in order to improve performance of the spectral method. In [Rodriguez et al., 2008], it also can be seen a quantitative method of evaluation of these strategies.
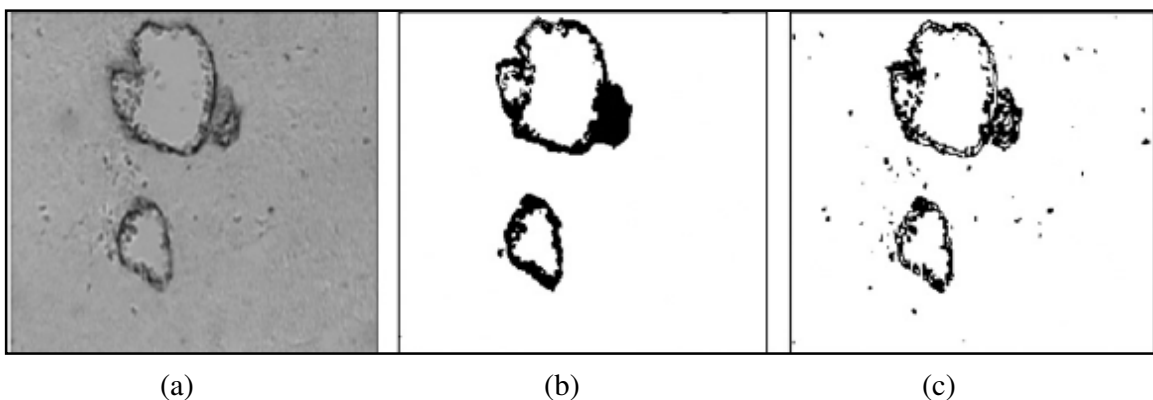

| (a) | (b) | (c) |

Fig. 34. (a) Original image, (b) Segmentation via the mean shift, (c) Segmentation via the spectral method

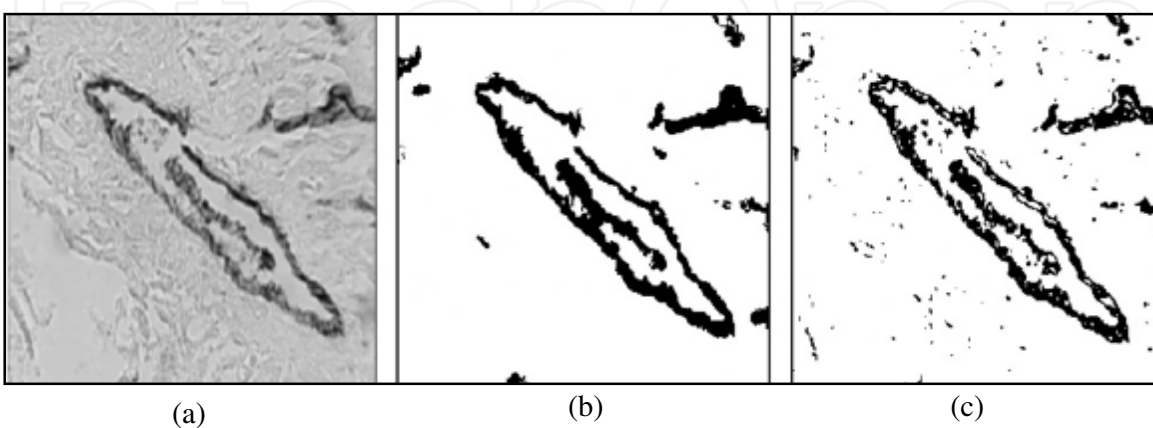| (a) | (b) | (c) |

Fig. 35. (a) Original image, (b) Segmentation via the mean shift, (c) Segmentation via the spectral method

5. Conclusions

In this chapter was carried out a brief theoretical introduction of the *Watershed* transformation. Through the experimentation suitable markers were obtained for the atherosclerotic lesions (including to the background). In such a sense, a new algorithm was introduced, which was efficient in order to mark the atherosclerotic lesions and to eliminate all other spurious information. With the proposed strategy the application of the watershed segmentation gave good results, where the exact contours of the objects of interest were obtained (atherosclerotic lesions). Furthermore, over-segmentation never was obtained.

A theoretical introduction of the mean shift was carried out too. In such a sense, a new algorithm was proposed for image segmentation of blood vessels. The same was suitable for this application. In order to demonstrate its good performance, the same one was compared with another segmentation algorithm already established (the spectral method). Through several experiments with real images, we proven that the segmented images by using the mean shift were less noisy than those attained by means of the spectral method. In addition, the obtained edges were better defined by using the mean shift than those attained by the spectral method.

The strategies introduced in this chapter can be extended to other types of biomedical images and their application is valid for other tasks of image analysis where suitable methods of segmentation are required.

6. References

Cheng, Y. (1995). Mean Shift, Mode Seeking, and Clustering, IEEE Transactions on Pattern Analysis and Machine Intelligence, Vol. 17, No. 8, (August 1995), pp.(790-799), ISSN: 0162-8828

Chin-Hsing, C.; Lee, J.; Wang, J. & Mao, C. W. (1998). Colour image segmentation for bladder cancer diagnosis, Mathematical and Computer Modelling, Vol. 27, No. 2, (January 1998), pp (103-120), ISSN: 0895-7177

Comaniciu, D. I. (2000). Nonparametric Robust Method for Computer Vision, Ph.D. thesis, New Brunswick, Rutgers, The State University of New Jersey, January, 2000.

Comaniciu, D. & Meer, P. (2002). Mean Shift: A Robust Approach toward Feature Space Analysis, IEEE Transaction on Pattern Analysis and Machine Intelligence, Vol. 24, No. 5, (May 2002), ISSN: 0162-8828

Cotran, R. (2002). Patología Estructural y Funcional, Mc. Grow Hill, México, ISBN: 970-10-2787-6.

Díaz-Flores, L.; Guitiérrez, R. & Varela, H. (1994). Angiogenesis. An update, Histoogy and Histopathology, Vol. 9, (July 1994), pp (807-853), ISSN 0213-3911

Fukunaga, K. & Hostetler, L. D. (1975). The Estimation of the Gradient of a Density Function, IEEE Transactions on Information Theory, Vol. IT-21, No. 1, (January 1975), pp. (32-40), ISSN: 0018-9448

Fernández-Britto, J. E.; Carlevaro, P. V.; Bacallao, J.; Koch, A.S.; Guski, H. & Campos, R. (1988): "Coronary atherosclerotic lesion: its study applying an atherometric system using principal components analysis". Z. Klin. Med. 44: 291-294, 1988.

Fernández-Britto, J. E. & Carlevaro, P.V. (1989). Atherometric System: Morphometric standardized methodology to study atherosclerosis and its consequences, Gegenbaurs morphologisches Jahrbuch, Vol. 135, (November 1989), pp (1-12), ISSN: 0001-5180

Fuh, C-S.; Maragos, P. & Vincent, L. (1991). Region based approaches to visual motion correspondence, Technical Report 91-18, (November 1991), pp (1-29), Harvard

Robotics Laboratory, Harvard University, Division of Applied Sciences, Pierce Hall, Cambridge NA 02138

Grenier, T.; Revol-Muller, C.; Davignon, F. & Gimenez, G. (2006). Hybrid Approach for Multiparametric Mean Shift Filtering, Image Processing, IEEE, International Conference, Atlanta, GA, 8-11, (Oct. 2006), pp (1541-1544).

Kenong, W.; Gauthier, D. & Levine, M. D. (1995). Live Cell Image Segmentation, IEEE Transactions on Biomedical Engineering, Vol.42, No. 1, (January 1995), pp (1-11), ISSN: 0018-9294

Koss, J.; Newman, F.; Johnson, D. & Kirch, D. (1999). Abdominal organ segmentation using texture transforms and a hopfield neural network, IEEE Transactions Medical Imaging, Vol. 18, No. 7, (July, 1999), ISSN: 0278-0062

Najman, L. & Schmitt, M. (1996). Geodesic Saliency of Watershed Countours and Hierarchical Segmentation, IEEE Transactions on Pattern Analysis and Machine Intelligence, Vol. 18, No. 12, (December 1996), pp (1163-1173), ISSN: 0162-8828

Otsu, N. (1978). A threshold selection method from grey level histogram, IEEE Transactions on Systems, Man and Cybernetics, Vol. SMC-8, No. 1, (January 1978), pp (62-66), ISSN: 0018-9472

Rodríguez, R.; Alarcón, T. & Sánchez, L. (2001). MADIP: Morphometrical Analysis by Digital Image Processing, Proceedings of the IX Spanish Symposium on Pattern Recognition and Image Analysis, Vol. I, pp (291-298), ISBN 84-8021-349-3, Spain.

Rodríguez, R.; Alarcón, T.; Wong, R. & Sanchez, L. (2002). Color segmentation applied to study of the angiogenesis. Part I, Journal of Intelligent and Robotic System, Vol. 34, No. 1, (May 2002), pp (83-97), ISSN: 0921-0296

Rodríguez, R.; Alarcón, T. & Pacheco, O. (2005). A New Strategy to Obtain Robust Markers for Blood Vessels Segmentation by using the Watersheds Method, Journal of Computers in Biology and Medicine, Vol. 35, No. 8, (October 2005), pp (665-686), ISSN: 0010-4825

Rodríguez, R. & Pacheco, O. (2007). A Strategy for Atherosclerosis Image Segmentation by using Robust Markers, Journal Intelligent & Robotic System, Vol. 50, No. 2, (October 2007), pp (121 – 140), ISSN: 0921-0296.

Rodríguez, R.; Castillo, P. J.; Guerra, V., Sossa, J. H.; Suárez A. G. & Izquierdo, E. (2008). A comparison between two robust techniques for segmentation of blood vessels, Journal of Computers in Biology and Medicine, Vol. 38, No. Issue 8, (June 2008). pp (931 – 940), ISSN: 0010-4825

Sijbers, J.; Scheunders, P.; Verhoye, M.; Van der Linden, A.; Van Dyck, D. & Raman, E. (1997). Watershed-based segmentation of 3D MR data for volume quatization, Magnetic Resonance Imaging, Vol. 15, No. 6, (February 1997), pp (679-688), ISSN: 0730-725X

Schmid, P. (1999). Segmentation of digitized dermatoscopic images by two-dimensional color clustering, IEEE Transactions Medical Imaging, Vol. 18, No. 2, February 1999), pp (164-171), ISSN: 0278-0062

Vicent, L. & Soille, P. (1991). Watersheds in digital spaces: An efficient algorithm based on immersion simulations, IEEE Transactins on Pattern Analysis and Machine Intelligence, Vol. 13, No. 6, (June 1991), pp (583-593), ISSN: 0162-8828

Vincent, L. (1993). Morphological grayscale reconstruction in Image Analysis: Applications and Efficient Algorithms, IEEE Transactions on Image Processing, Vol.2, No. 2, (April, 1993), pp (176-201), ISSN: 1057-7149

Weidner N.; Carroll, P. R.; Flax, J.; Blumenfeld, W. & Folkman, J. (1993). Tumour angiogenesis correlates with metastasis in invasive prostate carcinoma, American Journal of Pathology, Vol. 143, No. 2, (October 1993). ISSN: 0002-9440
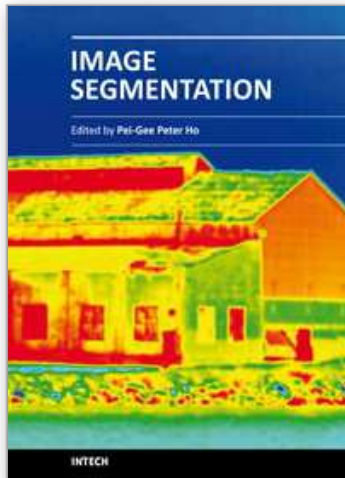
Image Segmentation

Edited by Dr. Pei-Gee Ho

It was estimated that 80% of the information received by human is visual. Image processing is evolving fast and continually. During the past 10 years, there has been a significant research increase in image segmentation. To study a specific object in an image, its boundary can be highlighted by an image segmentation procedure. The objective of the image segmentation is to simplify the representation of pictures into meaningful information by partitioning into image regions. Image segmentation is a technique to locate certain objects or boundaries within an image. There are many algorithms and techniques have been developed to solve image segmentation problems, the research topics in this book such as level set, active contour, AR time series image modeling, Support Vector Machines, Pixon based image segmentations, region similarity metric based technique, statistical ANN and JSEG algorithm were written in details. This book brings together many different aspects of the current research on several fields associated to digital image segmentation. Four parts allowed gathering the 27 chapters around the following topics: Survey of Image Segmentation Algorithms, Image Segmentation methods, Image Segmentation Applications and Hardware Implementation. The readers will find the contents in this book enjoyable and get many helpful ideas and overviews on their own study.

How to reference

In order to correctly reference this scholarly work, feel free to copy and paste the following:

Roberto Rodrîguez Morales (2011). Segmentation Methods for Biomedical Images, Image Segmentation, Dr. Pei-Gee Ho (Ed.), ISBN: 978-953-307-228-9, InTech, Available from: http://www.intechopen.com/books/image-segmentation/segmentation-methods-for-biomedical-images

INTECH
open science | open minds